buildings

MDPI

Review

Image-Based Quantitative Pore Analysis of Cementitious Materials: A Scale-Resolved Review of X-Ray CT Methods and Metrics

Minje Kim [1,†], Minjae Han [1,†], Sung-Chul Bae [2] and Heongwon Suh [1,3,*]

[1] Department of Architectural Engineering, Pusan National University, 2 Busandaehak-ro 63beon-gil, Geumjeong-gu, Busan 46241, Republic of Korea; minje3085@gmail.com (M.K.); mcky1108@pusan.ac.kr (M.H.)
[2] Department of Architectural Engineering, Hanyang University, 222 Wangsimni-ro, Seongdong-gu, Seoul 04763, Republic of Korea; sbae@hanyang.ac.kr
[3] Research Institute of Industrial Technology, Pusan National University, 2 Busandaehak-ro 63beon-gil, Geumjeong-gu, Busan 46241, Republic of Korea
* Correspondence: hwsuh125@pusan.ac.kr
† These authors contributed equally to this work.

Abstract

X-ray computed tomography (CT) has become the reference non-destructive technique for the three-dimensional characterization of the pore structures of cementitious materials. This review maps 140 application studies—spanning cement paste, mortar and concrete, from air-entrained, cellular and recycled-aggregate systems to alkali-activated binders, ultra-high-performance concrete (UHPC) and 3D-printed materials—and the underlying image-analysis methodology is inventoried separately and excluded from all frequency statistics. Each study is classified by voxel-size class (sub-micron, <1 μm; micro, 1–20 μm; meso, 20–100 μm; macro, >100 μm; multiscale), with voxel size being a sampling parameter rather than a spatial resolution, and by the pore metrics it reports under six metric families. The synthesis reveals similar concentrations at the micro (48/140) and meso (50/140) scales, a dominance of porosity and pore-size distribution at every scale, and pronounced under-use of higher-order shape and spatial statistics: flatness, elongation and pair-correlation functions each appear in less than 2% of studies. Systematic discrepancies between scales are analyzed: resolution-conditioned porosity, the representative elementary volume–resolution dilemma, segmentation-induced variance comparable to material effects, and the persistent CT–mercury intrusion porosity mismatch. Priorities are standardized segmentation benchmarks, scale-bridging registration protocols, routine uncertainty reporting and broader adoption of quantitative shape and spatial descriptors. Provisional assignments are flagged in the dataset.

Keywords: X-ray computed tomography; pore structure; cementitious materials; pore morphology; segmentation; representative elementary volume

Check for updates

Academic Editor: Yun Gao

Received: 18 September 2026
Revised: 3 October 2026
Accepted: 7 October 2026
Published: 10 October 2026

Copyright: © 2026 by the authors. Licensee MDPI, Basel, Switzerland. This article is an open access article distributed under the terms and conditions of the Creative Commons Attribution (CC BY) license.

1. Introduction

The pore structure of cementitious materials governs nearly every property of their engineering interest: compressive and tensile strength [1–3], elastic stiffness [4], permeability [5,6], sorptivity [7,8], freeze–thaw resistance [9,10], and the transport processes that drive reinforcement corrosion [11,12], carbonation [13,14], sulfate attack and alkali–silica reaction [15,16]. Pores in hardened-cement-based materials span an extraordinary size range—from nanometric gel pores within calcium–silicate–hydrate, through capillary pores

of tens of nanometers to a few micrometers, up to entrained and entrapped air voids of tens of micrometers to several millimeters, and finally to process-induced macro-defects such as honeycombing or the interlayer voids of 3D-printed elements [17,18]. No other microstructural feature of concrete covers roughly six orders of magnitude in size—nanometers to millimeters—while remaining relevant to performance at every one of them; of that full spectrum, the span accessible to CT at practical voxel sizes covers about four orders of magnitude, a distinction that recurs throughout this review.

Research on pore characterization is correspondingly extensive and continues to diversify across materials, exposure conditions and imaging modalities [19–21]. Across this large body of the literature, however, pore structure has most commonly been reported through amount- and count-type measures—total porosity, pore counts, and pore-size distributions—while richer quantitative descriptors of individual pores and their collective architecture (morphology, spatial arrangement, topology) have long remained secondary [19,20]. The importance of genuinely quantitative pore analysis has recently come to the fore: performance-relevant behavior is increasingly traced not to how much pore space exists but to how it is shaped, arranged and connected, and CT-based pore studies have grown rapidly in the past decade. Image-based analysis—above all, X-ray computed tomography—is the instrument class that makes this quantification possible in three dimensions while being non-destructive.

Conventional pore-characterization techniques each capture only a fragment of this spectrum, and each at a price. Mercury intrusion porosimetry (MIP) probes only mercury-accessible pathways, suffers from the well-documented ink-bottle effect that systematically misassigns pore volume to small pore sizes, requires severe drying, and destroys the specimen [22–24]. Gas adsorption addresses only the finest pores [22,25]. Optical and scanning electron microscopy provide exquisite local detail but reduce an inherently three-dimensional, connected network to two-dimensional sections, from which three-dimensional quantities can be inferred only through stereological assumptions that fail for the irregular, multiscale porosity of cementitious materials [22,26]. X-ray computed tomography (CT) removes these limitations in principle: it reconstructs the internal X-ray attenuation field of an intact specimen in three dimensions, non-destructively, and—with laboratory micro-CT now widely accessible and synchrotron beamlines, offering sub-micrometer resolution and time-resolved imaging—it has diffused into virtually every subfield of cement and concrete research, as summarized in subsequent reviews [19,20,27–29], following early cement-paste applications [26,30,31].

With this diffusion, however, has come fragmentation. Studies of the same nominal quantity—porosity, pore size, pore shape—are performed at voxel sizes ranging from tens of nanometers to several hundred micrometers, on specimens ranging from millimeter-scale paste fragments to full drilled cores, and with segmentation pipelines ranging from a single global threshold to trained convolutional networks [32–35]. The resulting numbers are frequently compared across studies as if they were equivalent, although each is conditioned on resolution, field of view, specimen size and processing choices. Review articles exist for individual subdomains: Brisard et al. [19] reviewed multiscale tomography of cementitious materials with emphasis on instrumentation and physics, Chung et al. [20] surveyed micro-CT applications in cement-based materials according to the property studied, and general CT reviews cover methodology across disciplines [27–29]. None of these, however, classifies the applied cementitious literature jointly by voxel-size class and by metric reported, or quantifies usage frequencies across that classification—a scale-explicit synthesis of what is actually measured, at which voxel size, with which metrics, and with which systematic incompatibilities is currently missing for cementitious materials. Three questions define that missing synthesis: (Q1) What is actually measured and at which voxel-size class?

(Q2) Why do nominally identical metrics disagree across scales and studies? (Q3) What minimum reporting would make them comparable?

This review addresses these three questions. Specifically, we (i) assemble a corpus of 140 peer-reviewed journal and conference publications applying X-ray CT to pore analysis of cement paste, mortar and concrete—the application corpus over which all frequency statistics in this review are computed—together with a separately inventoried set of cross-cutting methodological references; (ii) classify every application study by voxel-size class and by the pore-analysis metrics it reports under a six-family taxonomy; (iii) visualize where the literature concentrates and which metrics dominate at each scale; and (iv) analyze the discrepancies, incompatibilities and blind spots that emerge when the results are compared across scales. The scope is deliberately restricted to cementitious (cement-based) materials in the broad sense—Portland systems, blended and alkali-activated binders, and cement-based composites including foamed, pervious, fiber-reinforced and 3D-printed variants. The methodological literature, originating in other imaging communities, is cited strictly in its role as the source of algorithms that cementitious studies subsequently adopted [36–39]; non-cementitious and fiber-only examples provide an explicitly separate methodological context. Section 2 describes how the corpus was assembled and classified; Section 3 reviews the CT workflow and its intrinsic constraints; Section 4 establishes the metric taxonomy; Section 5 presents the scale-resolved landscape (Q1); Section 6 analyzes cross-scale discrepancies (Q2); Section 7 recasts the scale-resolved landscape by material domain (Q1, along the materials axis); Section 8 identifies research priorities and operationalizes minimum reporting through a metric-conditional checklist (Q3).

2. Corpus Assembly and Classification

The corpus underlying this review was assembled in July–August 2026 through topic-structured web searches of scholarly indexes and publisher databases—Google Scholar-type academic search, the major publisher platforms (including Elsevier ScienceDirect, Springer Nature, MDPI, Wiley, ASCE, RSC, IOP and Frontiers) and PubMed/PMC—organized across eight cementitious subdomains: cement paste and mortar; concrete durability and degradation; air-void and meso-scale concrete; pervious concrete; cellular, foamed and lightweight concretes; alkali-activated and geopolymer systems; ultra-high-performance concrete (UHPC) and fiber-reinforced composites; and 3D-printed cementitious materials; plus a cross-cutting image-analysis track. Search terms combined CT synonyms ('X-ray computed tomography', 'micro-CT', 'XCT', 'synchrotron tomography') with material terms (cement, mortar, concrete, and subdomain-specific vocabulary) and pore terms (pore, void, porosity). The literature coverage extends through mid-2026. Figure 1 summarizes the architecture of the review: the corpus, its classification, and the three outputs that the remaining sections develop.

Inclusion required (i) a peer-reviewed journal or conference publication in which (ii) X-ray CT—laboratory or synchrotron—is applied to a cementitious material and at least one quantitative pore metric is reported, or, for the separate methodology set, a cross-cutting image-analysis methodology adopted by such studies. Exclusion criteria were non-CT imaging modalities and non-cementitious applications; full-text verification removed ten initially collected studies—one using conventional photographic rather than CT imaging [40], eight whose pore analysis rests on MIP, nitrogen adsorption, nuclear magnetic resonance, scanning electron microscopy (SEM) or backscattered-electron (BSE) imaging without a CT experiment [25,41–47], and one applying CT to raw hemp shiv without a mineral binder [48]. A small number of retained studies concern mineral-binder systems at the margin of the cementitious family—gypsum plaster [49], lime–hemp concrete [50] and heritage mortars [51]—which were kept because their CT pore-analysis methodologies transfer directly and were flagged accordingly in the classified

dataset. Each application record was assigned to one of five material domains—cement paste and mortar; concrete at the meso and macro scales (air-void, pervious and recycled-aggregate concretes); concrete durability and degradation; advanced cementitious systems (alkali-activated and geopolymer binders, UHPC and fiber-reinforced composites, and 3D-printed materials; the last of which is assigned by processing route, according to whether the printed matrix is a mortar or a concrete); and cellular, foamed and lightweight concretes. Five domain-internal reviews [12,19–21,52] are likewise retained, classed as multiscale by convention, and flagged in the dataset because the metrics a review compiles document what the field reports at each scale; since reviews draw on primary studies, a limited overlap with individually catalogued records is possible, and its effect is quantified below. Eleven additional records on non-CT pore imaging, unbound constituents, qualitative CT illustrations or fiber-only characterization were moved to the separate methodological and contextual set. Their results remain cited where relevant, but their descriptors are not counted as CT pore metrics. The resulting application corpus comprises 140 studies, over which every frequency statistic and quantitative chart in this review is computed. The cross-cutting methodological references—thresholding and segmentation, network extraction, shape and tortuosity formalism, and general CT methodology, largely originating in other imaging communities—are inventoried separately in the same classified dataset and are cited throughout but not counted in any frequency statistic. One corpus study is co-authored by the corresponding author [1]; it was identified and coded under the same inclusion criteria as other records, while its voxel-size assignment remains provisional because its full text was unavailable.

Searches combined a CT term, a material term and a pore term—for example, ("X-ray computed tomography" OR "micro-CT" OR "XCT" OR "synchrotron tomography") AND (cement OR mortar OR concrete OR cementitious) AND (pore OR porosity OR "pore structure" OR "air void")—with a qualifier for each thematic track, such as AND ("air void" OR "freeze–thaw"), AND ("alkali-activated" OR geopolymer), AND ("3D printing" OR "additive manufacturing"), AND (UHPC OR "fiber-reinforced"), AND (pervious OR foamed OR lightweight), AND (segmentation OR thresholding OR "representative elementary volume") for the methodological track. The results were narrowed down in three stages: title-and-abstract screening against criteria (i) and (ii), full-text assessment of the retained records (the 206 catalogued references), and classification into the 140 application studies, 56 methodological and contextual records and the 10 exclusions listed above. Because the searches were run as structured queries across several platforms rather than as a single exportable database query, per-step record counts were not logged and a PRISMA-type flow cannot be reconstructed; the classified dataset instead records the final disposition and supporting evidence of every catalogued reference.

Each application record was assigned a voxel-size class using the finest CT voxel at which its pores or cracks were quantified: sub-micron (<1 μm), micro (1–20 μm, including both endpoints), meso (>20–100 μm) or macro (>100 μm). Studies combining multiple CT acquisitions of the same material system at different voxel sizes, including resolution-sensitive and local/full-volume scans, were classed as multiscale. Ordinary specimen-dependent changes within one acquisition protocol were assigned by the finest reported value; computational downsampling alone and combining CT with non-CT modalities do not establish multiscale CT. Domain reviews are retained in the multiscale category by convention, with no experimental voxel size attributed to the review itself. Metrics are assigned once per record to their class and coded against the 22-term vocabulary in Section 4; a review or multiscale row is not redistributed to the finest single-scale column. Bibliographic metadata and DOIs were checked for every retained record. Full texts were available for 177 of the 206 references, including 127 of the 140 application records, and the voxel size of every application record with an accessible full text was verified against the

source document. A numeric voxel or pixel size was located in the full texts of 106 records. The remaining 34 records were classed from the qualitative scale information available in their source (instrument class, stated resolution range or specimen size): 5 are domain reviews retained in the multiscale category by convention, and the other 29, together with 1 record whose reported unit is ambiguous, are flagged as provisional in the dataset (30 records). Two records deserve particular caution: one recycled-concrete study reports a cubed voxel unit that does not uniquely establish its edge length, and one multi-technique study provides no accessible evidence for more than one CT voxel size. Publisher- and domain-oriented search channels condition journal distributions and publication trends. The classified dataset and codebook, including evidence and uncertainty flags, are available from the corresponding author on reasonable request.

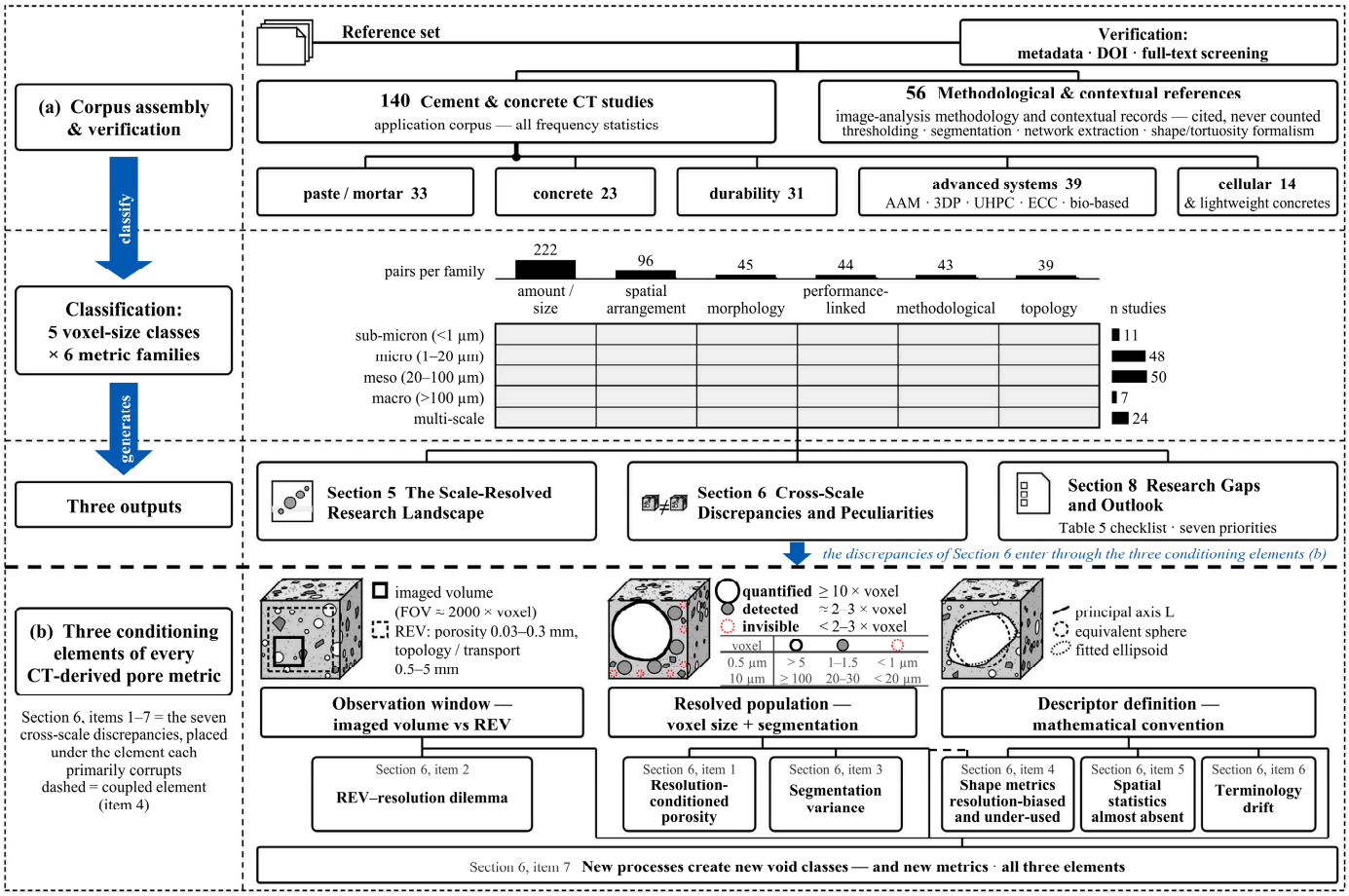

Figure 1. Framework of this review. (**a**) Corpus assembly and verification: 140 X-ray CT pore-analysis studies form the application corpus on which all frequency statistics are based, with 56 methodological and contextual references inventoried separately (cited, never counted); all records were screened by metadata, DOI resolution and, where available, full text. The corpus is classified by five voxel-size classes × six metric families (489 study–metric pairs; family and class counts as shown) and yields three outputs: the scale-resolved landscape, the cross-scale discrepancies and the reporting checklist with research priorities (Section 8). (**b**) The three conditioning elements of every CT-derived pore metric—the observation window (imaged volume versus the representative elementary volume, REV), the resolved population (pores quantified at ≥10× voxel, detected at ≈2–3× voxel and invisible below) and the descriptor definition (principal axis, equivalent sphere, fitted ellipsoid)—with the seven cross-scale discrepancies of Section 6 placed under the element each primarily corrupts; item 4 couples two elements and item 7 enters through all three.

Neither the provisional assignments nor the inclusion of reviews affects the results. Restricting the corpus to the 110 records with a source-verified voxel size preserves every ranking reported in Section 5: micro (35, 31.8%) and meso (35, 31.8%) remain the largest and comparable classes; amount and size metrics still account for 44.7% of study–metric pairs (45.4% in the full corpus) and spatial arrangement accounts for 19.0% (19.6%); and flatness, elongation and pair-correlation functions account for less than 2% of studies. Excluding the five reviews (135 studies) likewise changes no ranking—only the multiscale share falls from 17.1% to 14.1%, since the reviews sit entirely in that class—and excluding both groups (105 studies) preserves every ordering in Section 5.6.

Three limitations bound these statistics. First, coding was performed by a single coder with subsequent verification passes, so no inter-rater statistic is claimed; for the judgment-dependent terms—general pore shape, spatial distribution and connectivity—a term was recorded only where a study reported a quantity under that heading, and the dataset stores the evidence for every assignment so that any entry can be audited or re-coded. Second, a record was flagged as provisional when no numeric voxel size could be located in the accessible full text, when a cubic voxel unit left the edge length undetermined, or when the use of more than one voxel size could not be confirmed (30 of 140 records; their exclusion leaves the statistics unchanged, as shown above). Third, because a descriptor can be recorded only where a study reports it, rarely reported higher-order descriptors are more likely to be under- than over-counted, and the frequencies of the least common metrics are lower bounds. The statistics therefore describe a corpus coded under the stated criteria—not a census of the global literature—and support comparisons of relative emphasis rather than absolute counts.

3. X-Ray CT Workflow for Cementitious Pore Analysis

3.1. Acquisition and the Resolution–Field-of-View Trade-Off

Laboratory micro-CT and synchrotron tomography reconstruct a specimen from hundreds to thousands of radiographic projections acquired over a rotation of 180° or 360°. In cone-beam laboratory systems, spatial resolution is set jointly by focal-spot size, detector pixel pitch and geometric magnification; in parallel-beam synchrotron configurations, it is set by the detector optics. The single most consequential acquisition parameter is voxel size, which is inescapably bound to the field of view: for a detector of roughly 2000 pixels across, imaging a 100 mm concrete core yields voxels near 50 µm, while 1 µm voxels restrict the specimen to a few millimeters in diameter [19,27,29]. This coupling is strict only for full-specimen-in-field-of-view scanning: region-of-interest (local or interior) tomography images an interior subvolume of a larger specimen at high resolution, and detector-shift stitching extends the field of view at a fixed voxel size—but local tomography pays for this relaxation with truncation artifacts and non-quantitative reconstructed gray values that directly undermine the global-threshold segmentation most studies rely on [27–29]. Since capillary pores in hydrated paste extend well below 100 nm, no single scan can capture the full pore system of concrete: every CT study is implicitly a study of the pore subpopulation resolvable at its chosen scale [24,53,54]. Practical acquisition choices—tube voltage and filtration for sufficient penetration of dense aggregate, exposure and frame averaging for signal-to-noise, rotation-step count for angular sampling—further condition image quality and hence every downstream metric.

A caution applies to the organizing axis of this review itself: voxel size is a sampling parameter, not spatial resolution. In laboratory cone-beam CT, the point-spread function, set by focal-spot penumbra, detector unsharpness and the reconstruction filter, typically limits true spatial resolution to about 2–3 voxel widths at best, and reliable quantification demands substantially more: a feature spanning 2–3 voxels may be detected, but its volume, surface

and shape are dominated by partial-volume and discretization error until it spans roughly 10 voxels or more [27–29]; high-contrast features such as air voids and cracks are a partial exception, detectable—though not accurately measurable—below these multiples through partial-volume gray-level depression. The classes used throughout this review (Table 1) are therefore defined strictly by reported voxel size—the parameter which studies actually state—and Table 1 distinguishes the minimum detectable from the minimum quantifiable feature sizes per class. For the same reason, we label the finest class 'sub-micron' rather than 'nano': true nano-CT and ptychographic tomography, with spatial resolutions below roughly 150 nm, are distinct techniques with different optics, fields of view and artifact regimes, and sub-micron-voxel micro-CT resolves only the coarsest capillary porosity—no gel porosity is resolved at all. Figure 2 renders both constraints graphically: panel (a) shows the resolution–field-of-view–representative elementary volume (REV) trade-off, and panel (b) shows the pore-size spectrum against the windows of the principal complementary techniques (detailed in Section 4.1).

Table 1. Voxel-size classes and the cementitious pore features detectable and quantifiable at each. Voxel size is a sampling parameter: true spatial resolution is typically 2–3 voxel widths, and robust quantification of size and shape requires features spanning roughly 10 voxels or more (Section 3.1).

Class	Voxel Size	Typical Specimen	Void Features: Minimum Detectable/Minimum Quantifiable	Representative Applications
Sub-micron	< 1 µm	Paste fragments, $\lesssim$ 1–2 mm	Coarse capillary pores and hollow-shell voids from $\sim$ 2–3× voxels (sub-µm to $\sim$ 3 µm)/$\sim$ 10× voxels; gel and fine capillary porosity is invisible	Paste hydration, tortuosity, leaching [7,26,30,31]
Micro	1–20 µm	Paste/mortar, 1–10 mm	Entrained air, microcracks, interlayer voids, coarsest capillaries: $\sim$ a few µm–60 µm/$\sim$ 10–200 µm	Hydration and segmentation [55,56]
Meso	20–100 µm	Mortar/concrete, 10–100 mm	Air-void system, macro-pores, cracks: $\sim$ 40–300 µm/$\sim$ 0.2–1 mm; 10–50 µm small-void tail undetected	Air-void analysis, recycled-aggregate concrete (RAC), damage [57,58]
Macro	> 100 µm	Large specimens, cores, printed elements	Pervious macro-pores, honeycombing, large voids and cracks: $\sim$ 0.2–0.5 mm/$\sim$ 1 mm and above	Pervious concrete, large-element scanning [59–61]
Multiscale	Combined	Nested subsampling	Concatenated pore spectra across classes	Scale-bridging methodology [24,53,54]

The gap between voxel size and spatial resolution has two physical origins whose weight differs by instrument [27–29]. The first is the point-spread function: in cone-beam laboratory systems, the focal-spot penumbra, which grows with magnification, detector unsharpness and the reconstruction filter, together limit true resolution to about two to three voxel widths [27,28], whereas, in parallel-beam synchrotron configurations, the focal-spot term is absent and resolution approaches the voxel grid, while monochromatic illumination removes the beam-hardening cupping that distorts gray values in laboratory scans of aggregate-bearing specimens [26,29,62]. The second is the partial-volume effect: a voxel straddling a pore–solid interface records the attenuation average of both phases, so the segmented boundary depends on the threshold [32,34,63]. These effects propagate unequally into the metric families. Amount metrics are the most robust, because partial-volume voxels are divided between the phases and the errors partly compensate in a volume average; morphological descriptors are biased systematically, because the interface quantized onto the voxel grid overestimates surface area and depresses sphericity for pores spanning fewer than about ten voxels [28,63]; and topological descriptors are the most fragile, because a throat that is one or two voxels wide can be closed by the threshold—severing a percolating path—or opened by blurring between neighboring pores [24,54,64].

This asymmetry is why Table 1 states minimum detectable and minimum quantifiable sizes separately and why the reporting checklist of Section 8 requires every metric to be declared together with its voxel size.

Synchrotron sources add three capabilities that laboratory systems approach only partially: monochromatic beams that eliminate beam-hardening at the source, coherence that enables phase-contrast imaging of weakly absorbing features, and photon flux that compresses scan times from hours to seconds. The last enables in situ, time-resolved (often called 4D CT) imaging, exemplified by synchrotron tracking of early cement hydration [62]; synchrotron imaging has also linked pore structure to water absorption ex situ [7], and laboratory micro-CT porosity has been cross-validated against diffraction at a fixed hydration age [65]. Time-resolved imaging is no longer confined to synchrotrons; however, laboratory scanners have been used to observe the setting of adjacent mineral binders in situ [49], thermally driven moisture migration and capillary water uptake [8,66], and crack initiation and propagation under in situ loading [67–70]; meanwhile, repeated ex situ scanning of the same specimen has tracked freeze–thaw damage accumulation [9,71,72] and self-healing product growth inside cracks [73–77]. A typical analysis pipeline—specimen preparation, scanning, reconstruction, filtering, segmentation, feature labeling and metric extraction—is shared across virtually all of the corpus, which is precisely why choices made at each pipeline stage propagate into every reported number.

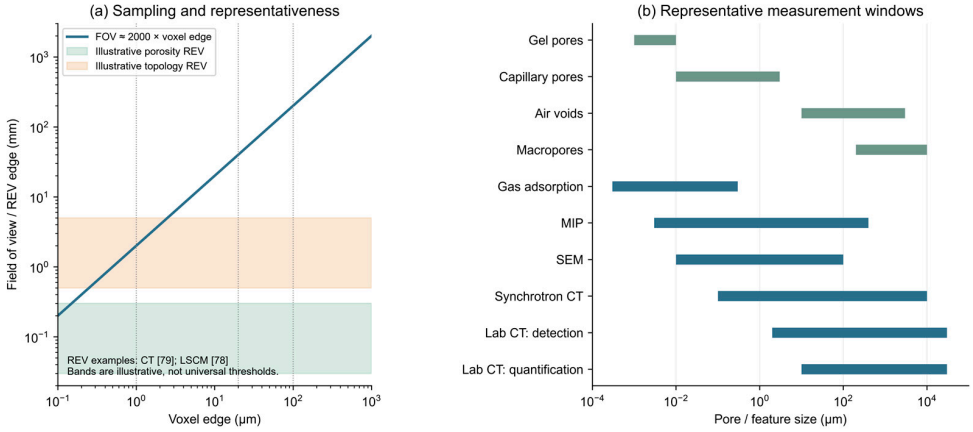

Figure 2. Measurement physics conditioning for every metric in this review. (**a**) Voxel size versus accessible field of view for full-specimen scanning (≈2000 detector pixels), with the voxel-size classes of Table 1: the field-of-view line assumes a 2000-pixel detector width (FOV ≈ 2000 × voxel edge), and the shaded bands are illustrative: the porosity-REV band (0.03–0.3 mm) covers the values reported for hardened paste by laser scanning confocal microscopy (LSCM; 35–100 µm cubes [78]) and the lower part of the range found by CT at 1–8 µm voxels (≈0.1–1 mm [79]), while the topology-REV band (0.5–5 mm) is an order-of-magnitude indication, since diffusion tortuosity and formation factor did not converge within the LSCM volumes [78]. At fine voxels, the accessible volume falls below the topology REV—the resolution–representativeness dilemma of Section 3.4. (**b**) Cementitious pore populations and the size windows of the principal techniques, rendered on a continuous size axis to expose their overlaps and gaps (tabulated with key limitations in Section 4.1); laboratory micro-CT detection (≈2–3× voxel) and robust quantification (≥10× voxel) are drawn separately; technique envelopes vary with instrument and specimen, and the laboratory-CT examples assume ≈1 µm voxels.

3.2. Reconstruction Artifacts and Preprocessing

Between acquisition and analysis stand reconstruction and image conditioning, whose artifacts are easily mistaken for microstructure. Beam hardening—preferential attenuation of low-energy photons in polychromatic laboratory beams—brightens specimen peripheries and can masquerade as a denser rim, biasing porosity profiles near surfaces; it is mitigated by physical filtration, immersion in a compensating medium whose attenuation

approximates the matrix, wedge or linearization calibration, and iterative polychromatic reconstruction [27,28]. Ring artifacts from miscalibrated detector elements imprint circular features that intersect the pore phase; metal or dense inclusions cast streaks; specimen motion blurs boundaries. Noise-reduction filtering (median, non-local means, anisotropic diffusion) trades noise against edge sharpness, directly affecting where a subsequent threshold places the pore–solid boundary. The methodological literature treats these steps at length [27–29,80], but applied cementitious studies rarely report them in reproducible detail—an early link in a chain of unreported degrees of freedom that Section 6 revisits.

3.3. Segmentation

Segmentation—labeling voxels as pore or solid (or as one of several solid phases)—is the dominant source of operator-dependent uncertainty in CT pore analysis. Global histogram thresholding, Otsu's criterion [38,81] above all, remains the most common choice across the corpus; local and adaptive schemes, indicator kriging [82,83], and watershed-based separation of touching voids [84,85] follow. Machine learning segmentation entered through random forest, autoencoder and convolutional approaches developed for tomographic imaging in adjacent fields [86–88]—with multi-level Otsu thresholding cross-validated against SEM remaining the reference point for multi-phase rock images [89]—and has been adopted rapidly for cementitious images since about 2020: semantic segmentation of strain-hardening composites [90], machine learning phase segmentation reviewed for 3D-printed cementitious materials [52], multiscale segmentation networks [35], and hybrid physics-informed schemes [56,91]. Deep-learning approaches to cementitious microstructural image analysis broadly are reviewed by Qian et al. [92]. Table 2 summarizes the main segmentation families used on cementitious CT images and the porosity sensitivity that comparative studies attribute to the choice among them. The comparisons agree on an uncomfortable conclusion: the segmentation technique alone shifts measured porosity by several percentage points on identical images [34,93,94]—a spread of the same order as many of the mixture and curing effects that applied studies set out to resolve—and criterion choice can produce far larger, specimen-dependent divergence in reported void ratios [32]; for multi-phase hydrate quantification, the choice between global and local schemes likewise changes measured phase volumes by tens of percent in relative terms [33]. Partial-volume voxels at pore boundaries, and porosity below the resolution limit, bias all downstream metrics in ways that can be estimated but rarely are [63,91]. Figure 3 illustrates the canonical route from a grayscale CT slice through volume reconstruction to the threshold-segmented three-dimensional pore space [95].

Table 2. Principal segmentation families applied to cementitious CT images and their reported influence on measured porosity.

Family	Representative Methods	Reported Porosity Sensitivity	Key References
Global thresholding	Otsu, iterative/ISODATA, histogram decomposition	Spreads between criteria on identical images, from several percentage points to extreme, specimen-dependent divergence	[32,38,93]
Local/adaptive	Adaptive window, indicator kriging, hysteresis	Improves boundary fidelity; parameter-sensitive; roughly halves phase-quantification error versus global schemes	[33,34,82,83]
Region/marker-based	Watershed separation of touching voids	Alters pore counts and pore-size distribution (PSD) rather than total porosity	[84,85,96]

Table 2. *Cont.*

Family	Representative Methods	Reported Porosity Sensitivity	Key References
Machine/deep learning	Random forest, convolutional neural network (CNN), U-Net semantic segmentation	High accuracy on training-like data; annotation-dependent	[35,87,90,97,98]
Physics-informed	Gradient-based phase segmentation [56]; sub-resolution grayscale models [63]; hydration-stoichiometry (Powers model) inference from segmented unhydrated cement [91]	Recovers part of sub-voxel porosity	[56,63,91]

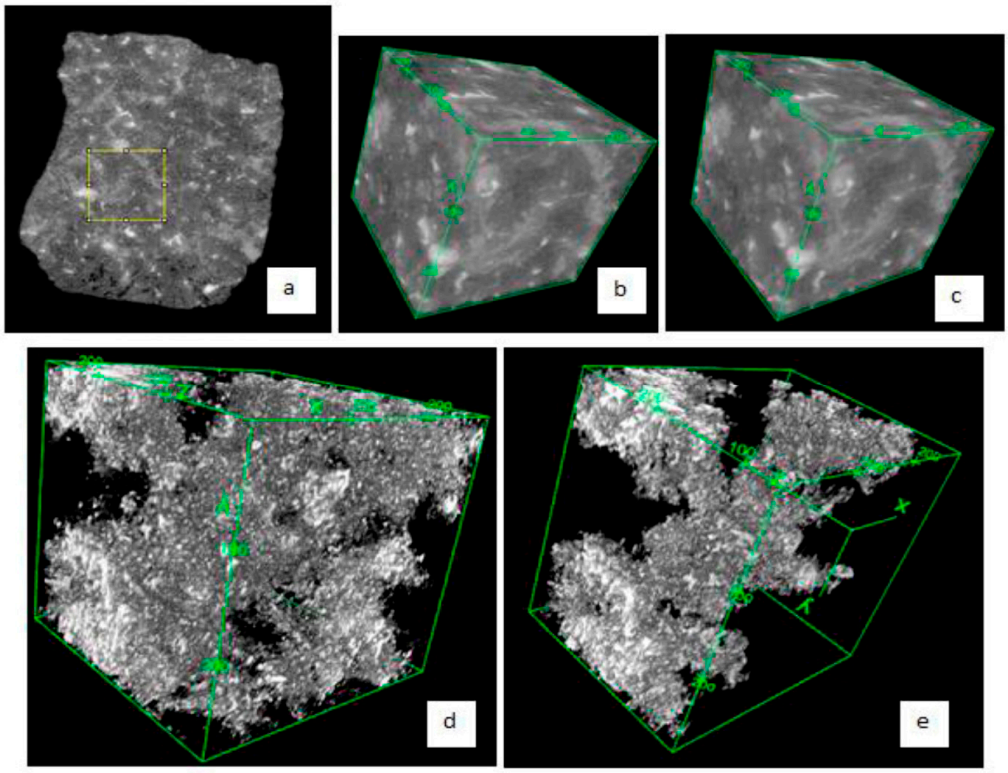

Figure 3. Pore segmentation workflow for a deteriorated cement paste: (**a**) an 8-bit representative slice (2000 × 2000 voxels) obtained from specimen OPC-de2 (ordinary Portland cement, OPC); (**b**) the volume of interest (VOI, 300^3 voxels) extracted from the normalized dataset; (**c**) the resulting 3D stack after denoising; (**d**) 3D visualization of the segmented total porosity of the VOI; (**e**) 3D visualization of the largest percolating pore cluster in the VOI, i.e., the effective porosity. Reproduced from Promentilla et al. [95], *Materials*, open-access (CC BY 4.0).

Three obstacles specific to cementitious CT separate the rapid adoption of learning-based segmentation from its validated use. The first is data: unlike the digital-rock and biomedical communities, which have assembled benchmark image sets [86,87,97,98], cementitious CT has no public expert-annotated dataset of appreciable size [92], so networks are trained on in-house labels produced by the thresholding procedures whose variance they are meant to remove, and the label rather than the architecture sets the accuracy ceiling. The second is gray-value physics: the attenuation distributions of capillary pores, hydrates, residual clinker and aggregate overlap and shift with beam hardening, specimen thickness and hydration age [33,56,91], so a model trained on one mix, scanner and voxel size degrades under domain shift in ways that held-out validation on the same dataset cannot reveal. The third is specificity: architectures developed for natural or biomedical images treat the pore space as a generic foreground class [98], whereas cementitious analysis depends on preserving thin throats and percolating paths, to which voxel-wise

accuracy and Dice-type scores—the measures reported in the cementitious applications so far [35,52,90]—are largely insensitive. Transfer to a new cementitious system therefore calls for validation on independently annotated data from a different scanner and mix, reporting of connectivity-preserving measures alongside voxel-wise ones, and an explicit statement of how the training labels were generated; the public benchmark identified as Priority (1) in Section 8 is the precondition for all three.

3.4. Representative Elementary Volume and Voxel-Size Effects

A metric is material-representative only if evaluated over a representative elementary volume (REV)—the smallest volume whose value converges to that of the bulk [4,79,99,100]. Cement-paste REV studies include CT analyses of hydration-dependent grayscale and phase statistics [79] and serial-section laser scanning confocal microscopy (LSCM) of pore geometry [78]; the latter reports metric-dependent convergence at cubes of tens to hundreds of micrometers and must not be presented as a CT measurement, whereas connectivity, tortuosity and other topological quantities require substantially larger volumes because they depend on rare percolating pathways [54,78]. Because finer voxels shrink the affordable field of view, resolution and representativeness are in direct conflict—the central dilemma of CT pore analysis [54,78,101]. Voxel-size sensitivity studies on cementitious materials demonstrate systematic loss of fine porosity and apparent pore-size inflation as voxel size coarsens [24,54,64], with connectivity metrics degrading fastest; grayscale-based methods for estimating lost sub-resolution porosity have been demonstrated on other porous ceramics and may transfer to cementitious systems, although validation on hydrating, multi-phase cement—with unhydrated clinker at high attenuation—is still needed [63]. The practical consequence is that a reported porosity is meaningful only jointly with its voxel size, specimen volume and segmentation route—a triplet that a substantial fraction of the applied literature does not fully report.

The REV is metric-specific, and the order matters in practice [99,100]. Porosity, a volume average of a densely sampled phase, converges first—within cubes of tens to a hundred micrometers in hardened paste [78] and at roughly 0.1–1 mm for CT at 1–8 µm voxels [79]; pore-size distributions converge more slowly because their upper tail depends on rare large voids [101]; spatial descriptors require volumes several times the characteristic object separation and are sensitive to edge effects; and topological quantities converge last, because connectivity and tortuosity depend on rare extended pathways—diffusion tortuosity and formation factor did not converge in volumes in which porosity had long stabilized [54,78]. The risk is therefore specific: a fine-voxel scan with a field of view of a few hundred micrometers can yield a defensible porosity while the connectivity computed on the same volume describes that subvolume rather than the material, and because the bias is systematic, repeating the scan does not expose it.

A convergence test is available without additional acquisition [99,100]: the metric is recomputed on concentric subvolumes of increasing edge length and reported as representative only if it reaches a plateau—for example, less than 5% variation across the final doubling of edge length—that is reproduced on several non-overlapping subvolumes of that size; otherwise, it should be reported as a subvolume value together with its analyzed dimensions. Expressing the analyzed volume as a multiple of the largest feature it contains, such as the d90 of the measured pore-size distribution, makes this judgment transferable between studies, which is why the reporting checklist of Section 8 asks for the analyzed volume and REV status with every metric.

3.5. Phase Discrimination, Contrast Enhancement and Correlative Techniques

Several acquisition and correlation techniques extend the basic workflow and deserve explicit mention because each alters what downstream pore metrics mean. Dual-energy or spectral CT acquires data at two tube voltages (or with energy-resolving detectors) to separate phases of similar gray value and reduce beam-hardening bias; it is established in general and geoscience CT methodology [27–29] but remains rare on cementitious materials. Contrast-enhanced pore imaging fills accessible porosity with a highly attenuating medium—Wood's metal intrusion, or cesium/brine doping of the pore solution—rendering connected or sub-resolution porosity visible; cesium-based contrast underpinned time-lapse imaging of alkali–silica reaction products in concrete [15]. At synchrotrons, propagation-based phase contrast with single-distance Paganin-type retrieval [102] is the workhorse for weakly absorbing hydrates, but the edge-enhancement fringes it exploits (and incompletely removes) systematically bias threshold placement at pore boundaries, so the retrieval settings belong with the segmentation metadata. Specimen moisture state matters for the same reason: pore water raises pore-phase attenuation, shifting histograms and threshold positions, so drying protocol and saturation state should accompany any quantitative scan—particularly in 4D hydration and moisture-transport studies. Prolonged synchrotron irradiation can additionally perturb hydrating specimens through radiolysis and local heating—a confounder that in situ 4D hydration studies need to control for. Finally, repeat-scan and load-stage studies rest on image registration: rigid or affine alignment of scan pairs suffices for differential pore metrics, whereas digital volume correlation (DVC) resolves internal displacement and damage fields; corrosion, freeze–thaw, load-stage and interface studies in this corpus employ these techniques [11,70,103,104], though registration accuracy is rarely reported.

3.6. The Software Ecosystem

The analysis stage runs on a small, shared toolset. Commercial platforms (Avizo, VGStudio, Dragonfly, CTAn) dominate applied cementitious studies, while open tools—ImageJ/Fiji with BoneJ for connectivity and anisotropy [105], PoreSpy for network extraction and metric batteries [106], and assorted MATLAB codes such as TORT3D for tortuosity [107]—carry most methodological work. The division matters for reproducibility: commercial pipelines embed proprietary defaults (surface smoothing, small-pore filters) that are rarely reported, whereas open pipelines are scriptable and auditable. Corpus studies trace part of the inter-study porosity scatter to analysis settings—threshold selection above all—that are chosen arbitrarily or left unreported [20,32,108]; Koenig notes that, in most μXCT pore studies, the procedure by which results are generated is not transparently described and no variances or reference values are given [108]. We extend this observation to the proprietary defaults of commercial pipelines. Movement toward open, versioned analysis scripts—normal practice in neighboring computational fields—would remove one of the cheapest-to-fix sources of irreproducibility in cementitious CT work.

4. A Taxonomy of Pore-Analysis Metrics

The metrics reported across the corpus organize naturally into six families (Table 3). This section defines each family and summarizes its usage on cementitious materials; Section 5 crosses the families with voxel-size class.

Table 3. Taxonomy of pore-analysis metrics used in X-ray CT studies of cementitious materials. The 22-term coding vocabulary of Section 2 maps onto the rows of this table, with combined descriptors (flatness/elongation; throat size/coordination number) coded as separate terms; the full token-to-row correspondence is given in the codebook accompanying the dataset (available from the corresponding author on reasonable request). Here, n is the total across all classes. All scales denote rows with $n \geq 20$ and nonzero counts in every class; for all other rows, the classes contributing at least 25% of that row are listed. Key references list every application record for rows with $n \leq 8$ and, for larger rows, one representative record per voxel-size class ("e.g.,").

Family	Metric	Definition/Typical Formulation	Dominant Scale(s) (Application Corpus, n = Study–Metric Pairs)	Key References
Amount/size	Porosity	Pore–voxel volume fraction of total volume	All scales (n = 120)	e.g., [2,7,10,16,59]
	Pore-size distribution	Equivalent-diameter or local-thickness histogram of pores	All scales (n = 98)	e.g., [2,7,10,16,59]
	Specific surface area	Pore–solid interface area per unit volume	Micro, multi (n = 4)	[22,23,81,108]
Morphology	Pore shape (general)	Unstandardized or qualitative shape reporting (2D form factors, visual classes) not reducible to the descriptors below	Meso, micro (n = 26)	e.g., [2,51,52,59]
	Sphericity	Surface area of volume-equivalent sphere/actual pore surface	Meso, micro, macro (n = 4)	[51,58,59,109]
	Flatness/elongation	Principal-axis ratios (S/I, I/L) of fitted ellipsoids	Micro, macro (n = 4)	[1,59]
	Aspect ratio	Longest/shortest axis of best-fit ellipsoid	Meso, micro (n = 3)	[2,110,111]
	Fractal dimension	Box-counting or PSD-slope self-similarity exponent	Meso (n = 8)	[5,71,109,112–116]
Spatial arrangement	Void spatial-distribution mapping	Density maps and depth/radial porosity profiles of void positions relative to a reference surface or phase	All scales (n = 79)	e.g., [9,12,16,26,59]
	Powers spacing factor	Index of the maximum distance from any point in the paste to the periphery of the nearest air void, computed from air content and void-specific surface under an idealized equal-void lattice model (ASTM C457)	Micro (n = 7)	[10,72,81,108,117–119]
	Nearest-neighbor distance	Distance statistics between pore centroids	Micro (n = 2)	[118,119]
	Radial distribution function	Pair correlation g(r) of pore centroids	Micro (n = 2)	[1,119]
	Anisotropy/orientation	Directional pore-fabric measures (mean intercept length (MIL), orientation tensors)	Meso (n = 6)	[2,120–124]
Topology/ connectivity	Connectivity	Connected fraction, Euler number, percolation check	All scales (n = 26)	e.g., [6,7,21,59,111]
	Tortuosity	Path-elongation measure; geometric, hydraulic, diffusive and electrical variants are inequivalent, and the τ vs. τ^2 convention varies [125–127]	Sub-micron (n = 10)	e.g., [5,7,21,60,111]
	Throat size/coordination number	Constriction size and bonds per pore from network models	Meso (n = 3)	[5,6]
Performance-linked	Permeability prediction	Stokes/lattice-Boltzmann (LBM) or network flow simulation on segmented pores	Meso (n = 10)	e.g., [5,21,61,95,128]
	Crack metrics	Crack volume, width, orientation, surface from damage imaging	Micro, meso (n = 34)	e.g., [11,12,18,114]
Methodological	REV	Smallest volume whose metric converges to the bulk value	Multi, meso (n = 5)	[4,19,54,79,129]
	Segmentation method	Global/local thresholding, watershed, machine/deep learning	Micro, meso (n = 38)	e.g., [9,12,26,55]

4.1. Amount and Size Metrics

Porosity—the pore–voxel fraction of total volume—is the universal baseline, reported in the overwhelming majority of studies at every scale. Pore-size distribution (PSD) follows closely, computed either on labeled discrete pores via equivalent spherical diameter, or on the connected pore space via local thickness (largest inscribed sphere), continuous PSD, or granulometry by morphological opening; these definitions are not interchangeable, and the corpus rarely states which is used—a quiet source of cross-study scatter [19,20,85,130]. Figure 4 shows a representative CT-derived PSD of a geopolymer foam—an advanced cementitious system with a cellular void structure—with the D10/D50/D90 (10th, 50th and 90th percentile diameter) descriptors commonly extracted from it. Specific surface area of the pore–solid interface, sensitive to both resolution and smoothing, appears mainly in paste-scale and methodological studies [22,28,106,108]; it is also estimator-dependent—voxel-face counting overestimates the area of smooth interfaces relative to marching-cubes or smoothed-mesh estimators [28] (by a factor approaching 1.5 for a digitized sphere, because summing face areas measures $|nx| + |ny| + |nz|$ of the local normal rather than unity), correspondingly deflating any sphericity computed from it—so cross-software comparison requires the surface estimator to be stated. Because every technique sees a different pore subpopulation, CT-based amount/size metrics must be interpreted against the complementary windows of MIP, gas adsorption and electron microscopy (Table 4): CT sees large pores that mercury misassigns to small radii through ink-bottle percolation [22–24], while MIP accesses fine porosity far below CT resolution. The techniques therefore bracket, rather than duplicate, the true distribution.

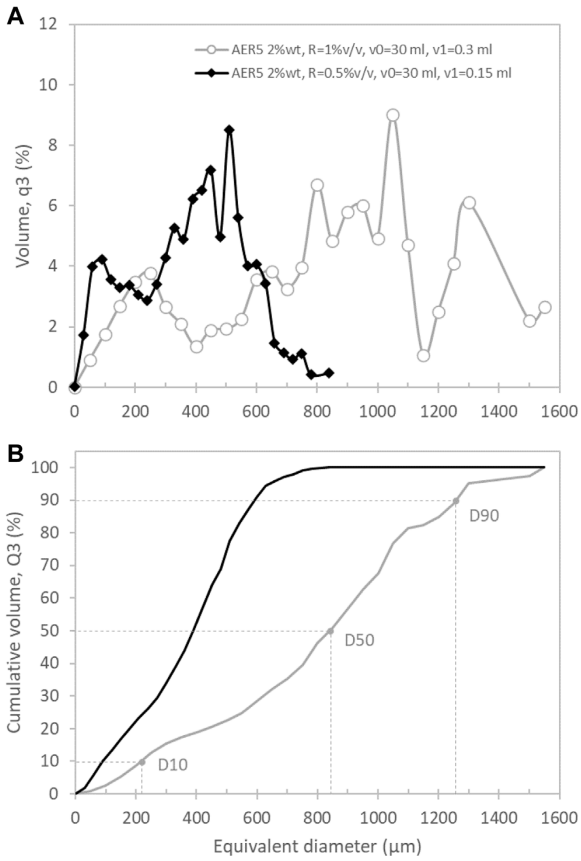

Figure 4. CT-derived pore-size distribution of a geopolymer foam: (**A**) differential (q3) and (**B**) cumulative (Q3) volume distributions for two foam formulations differing in blowing-agent ratio (R = 1% v/v, gray circles; R = 0.5% v/v, black diamonds); D10, D50 and D90 are marked on the cumulative curve of the R = 1% formulation. Adapted from Petlitckaia et al. [131], *Frontiers in Chemistry*, open-access (CC BY 4.0).

Table 4. Complementary windows of the principal pore-characterization techniques for cementitious materials.

Technique	Accessible Size Range	Dimensionality	Key Limitations	Complementarity with CT
X-ray CT	Feature detection from ~1 to 2 µm, robust quantification from ~5–10 µm to tens of mm (lab); detection to ~100–300 nm (synchrotron/lab nano-CT); the resolvable feature size is typically 2–3× voxel size, not the voxel size itself (high-contrast features such as cracks can be detected below this limit through partial-volume contrast)	3D, non-destructive	Resolution–field-of-view (FOV) bound; segmentation uncertainty	—
MIP	~3 nm–400 µm (accessible)	Bulk, indirect	Ink-bottle effect; drying damage; destructive	Covers sub-CT porosity; overlaps at coarse capillaries [23,24]
Gas adsorption	~0.3–300 nm	Bulk, indirect	Fine pores only; drying-sensitive	Anchors the nano end of the spectrum [22]
SEM/BSE image analysis	~10 nm–100 µm (2D)	2D sections	Stereological inference; surface preparation	Independent phase-fraction cross-check for CT segmentation [22,26]; overlaps CT at the coarsest capillaries [26]

4.2. Morphology Metrics

Morphological metrics characterize individual pores. Sphericity—commonly the Wadell ratio of the surface area of a volume-equivalent sphere to the actual pore surface—is the most used descriptor of individual pore shape in cementitious work [51,58,59,109]; fractal dimension, a population-level descriptor, is reported more often (eight records versus four, Table 3; see also Section 5.3). Flatness and elongation derive from the principal axes ($L \geq I \geq S$) of the best-fit ellipsoid or the eigenvalues of the pore's inertia tensor, typically as S/I and I/L respectively, following shape conventions formalized for particles [132] and adapted to three-dimensional pore spaces [133]; in the application corpus, they appear in two studies—a pervious-concrete study with large, well-resolved voids [59] and the authors' nanomaterial-modified paste study [1]—and Section 5.6 also reports how these tallies change if the two non-cementitious methodology sources that formalized them [132,133] are counted. Conventions moreover vary across the literature—Zingg-type axis ratios, $1 - S/I$ indices, L/I elongation—so that values near 1 denote equant pores under the convention used here, and cross-study comparison requires checking which convention was applied [132]. Aspect ratio condenses the same information into a single number and appears in foamed-concrete work [2] and in 3D-printing studies, where elongated interlayer voids are diagnostic of the process [110,111]. Fractal dimension—via box counting on the binary pore phase or from the slope of the cumulative PSD—serves as a global complexity measure, correlates empirically with strength and permeability in several cementitious studies [112,113], and has been used as an index of freeze–thaw damage state [71,114], though its physical interpretation across different computation routes remains debated [134,135]. A recurring weakness is that shape metrics are computed on pores only a few voxels across, where discretization noise dominates; very few studies state a minimum-voxel threshold for shape analysis; reported practice suggests safe thresholds of roughly 10 to 30 voxel diameters depending on the metric and the surface estimator, though these multiples are rules of thumb rather than derived limits. The principal-axis construction and the resulting shape classes in the flatness–elongation plane are illustrated in Figure 5 [1].

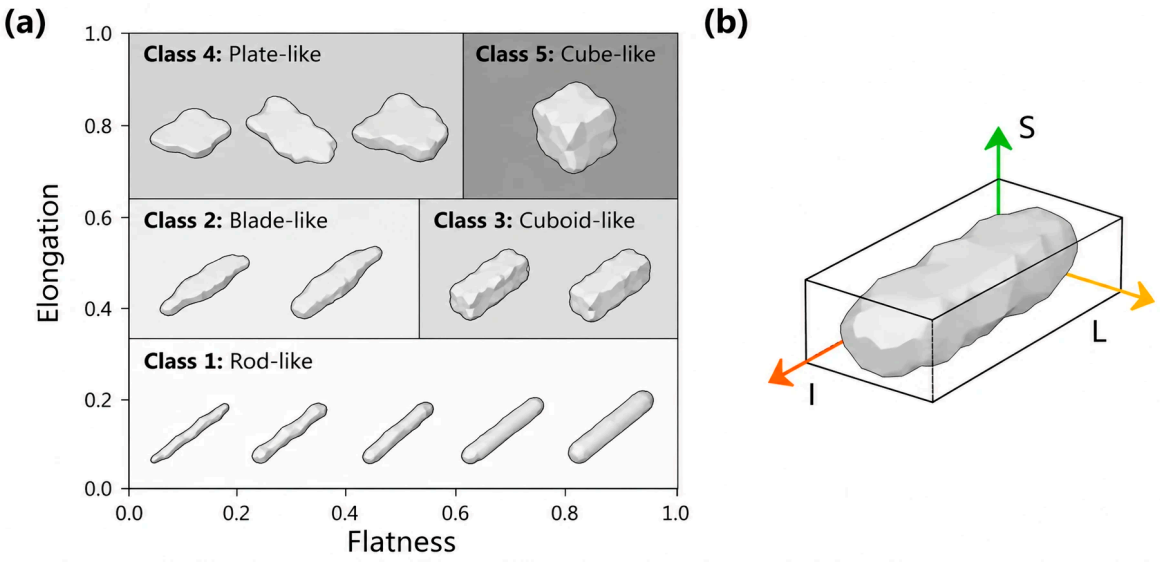

Figure 5. Zingg shape classification and equivalent ellipsoid representation of pore geometry: (**a**) classification of pore shapes in the flatness–elongation plane and (**b**) equivalent ellipsoid defined by the principal axes L ≥ I ≥ S. Illustration based on the methodology described in Suh et al. [1].

4.3. Spatial-Arrangement Metrics

Spatial metrics characterize where pores sit relative to one another and to other phases. The Powers spacing factor, inherited from ASTM C457 air-void practice, is the canonical example: an index of the maximum distance from any point in the paste to the periphery of the nearest air void, computed from the paste–air volume ratio and the void-specific surface under an idealized equal-sized-void lattice model. Two CT-derived quantities must be distinguished here: (i) the Powers index computed by inserting CT-measured air content and specific surface into the C457 formulae [10,81,108,117,118], and (ii) direct three-dimensional paste–void proximity (distance-transform) distributions [118,119]. They are not the same quantity—the Powers index is a model-based bound, the proximity distribution an actual geometry—and comparisons between them, and between either and linear-traverse results, show systematic offsets [118,119]. CT-based air-void characterization is maturing into a candidate alternative to the linear-traverse standard, although its validation so far rests on single-laboratory comparisons (Section 7.2). Nearest-neighbor distance statistics between pore centroids quantify clustering and repulsion [118,119]. The radial distribution function (RDF; pair correlation g(r)) generalizes nearest-neighbor statistics to all inter-pore distances and is standard in particle-packing physics, yet appears only twice in the cementitious corpus—for air voids in mortar [119] and for capillary-scale pores in nanomaterial-modified pastes before and after carbonation [1]. Directional descriptors—orientation tensors, mean intercept length, star-length distributions—quantify fabric anisotropy and have surged with 3D printing and fiber reinforcement, where extrusion aligns both fibers and interlayer voids [120,121,136–140], with applications extending to cellular concretes [2]. Distance-based mappings of porosity relative to a reference surface (depth profiles from an exposed face, radial profiles around aggregates or reinforcement) support degradation studies [71,141] and interfacial-transition-zone (ITZ) characterization [103,142]. Beyond pair statistics, the broader spatial-point-process toolbox—Ripley's K and L functions for clustering across all length scales and marked point patterns in which each pore carries its size or shape as a mark [143]—remains essentially untouched in cementitious CT work, although it ports directly to labeled pore centroids and would let arrangement hypotheses (clustering near aggregates, repulsion between entrained voids) be tested formally rather than described qualitatively. Figure 6 illustrates the g(r) construc-

tion for labeled pore centroids and its characteristic signatures for random, clustered and ordered arrangements [1].

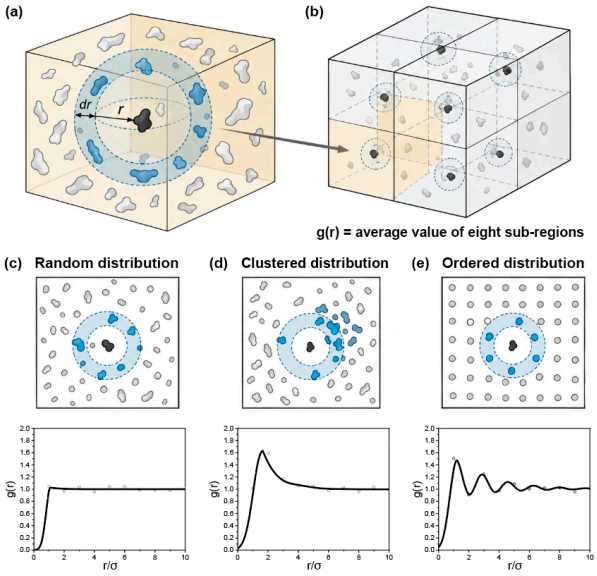

Figure 6. Conceptual illustration of the radial distribution function, g(r), for pore centroids: (**a**) spherical shell of radius r and thickness dr around a reference pore; (**b**) averaging of g(r) over eight subregions of the analyzed volume; and (**c**–**e**) two-dimensional illustrations of random, clustered, and ordered pore distributions, respectively. Illustration based on the methodology described in Suh et al. [1].

4.4. Topology and Connectivity Metrics

Topological metrics describe how the pore space is wired. Connectivity is reported variously as the connected (percolating) fraction of porosity, the Euler characteristic per unit volume, or a binary percolation check between opposite faces [30,53,60,78,144]; component-count (β0-based) and Euler-characteristic (χ-based) reporting are not interchangeable, since χ combines the three Betti numbers and a negative Euler density signals loop dominance rather than a large, connected fraction. Tortuosity quantifies path elongation through the pore network and links microstructure to transport coefficients, but it is not one quantity: geometric (geodesic) tortuosity from shortest paths, hydraulic tortuosity from simulated flow fields, diffusive tortuosity from effective-diffusivity ratios, and electrical tortuosity from formation factors are inequivalent definitions that yield systematically different values on identical geometries [125–127]. A further convention ambiguity—whether 'tortuosity' denotes the path-length ratio, τ, or the tortuosity factor, τ^2—produces factor-scale discrepancies between studies reporting nominally the same metric [125,126]. In the cementitious corpus, geometric/geodesic and diffusion-derived (random-walk) definitions dominate [7,21,30,60,95,145], and MIP-equation-derived tortuosity is additionally reported alongside CT metrics in the same study [111]—one more definitional stratum to check before comparison, and few studies state definition and convention explicitly—precisely the kind of cross-study incompatibility this review exists to expose. Throat size, pore-body size and coordination number derive from pore-network models extracted by maximal-ball [36,39,146,147] or watershed-based algorithms such as SNOW (subnetwork of an over-segmented watershed) [37,96,148]; these algorithms originated outside cement research and were ported wholesale into it [5,148]. Network metrics inherit every upstream uncertainty—segmentation, resolution, REV—and add algorithm dependence of their own: maximal-ball and watershed extractions can produce materially different coordination-number distributions from identical images [37,96]. Figure 7 illustrates the random-walk

approach: the trajectory of a walker diffusing through the CT-segmented pore space of a deteriorated paste, from which a diffusion-based tortuosity is estimated [95].

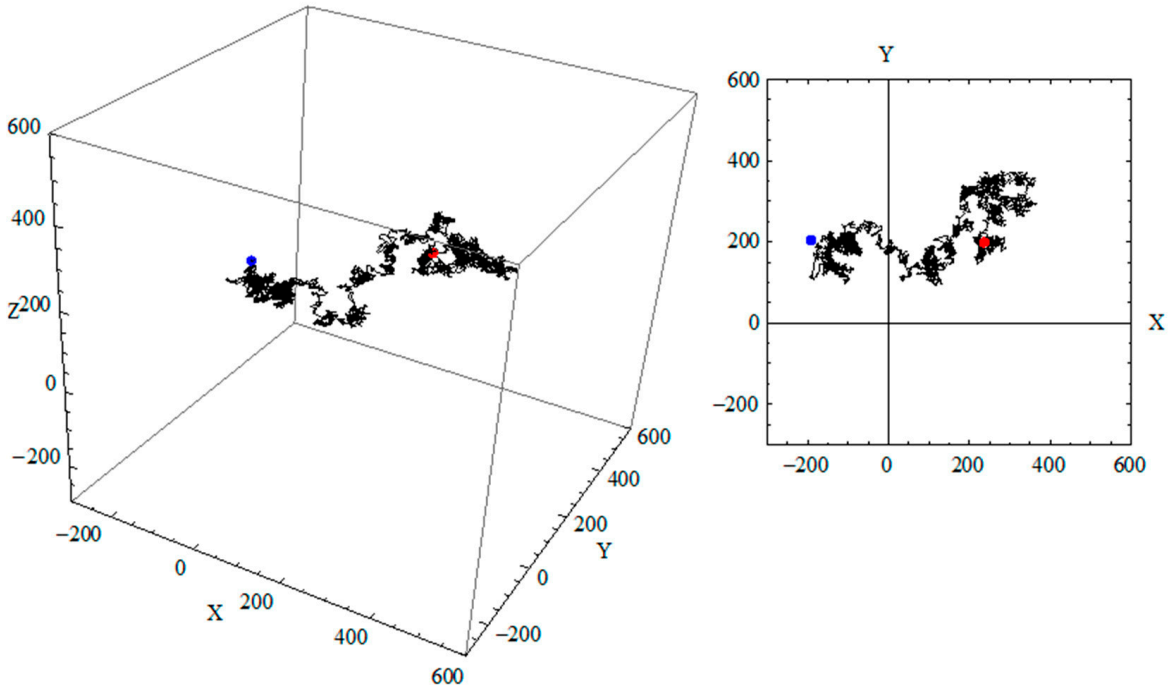

Figure 7. Random-walk tortuosity simulation in a CT-segmented pore space. Random-walk simulation of tortuosity in the CT-segmented pore space of a deteriorated cement paste: three-dimensional trajectory of a single walker and its planar projection (dots mark the start and end of the trajectory), from which the diffusion-based (random-walk) tortuosity is estimated—a diffusive quantity, distinct from the geometric (geodesic) tortuosity defined from shortest paths (Section 4.4). Adapted (cropped) from Promentilla et al. [95], *Materials*, open-access (CC BY 4.0).

4.5. Performance-Linked Metrics

A growing fraction of studies closes the loop from imaged pore space to predicted or measured performance. Permeability prediction runs Stokes or lattice-Boltzmann flow or network flow models directly on the segmented pore space, with reasonable success for pervious and foamed concretes whose transport-controlling pores are fully resolved [5,6,61,128,149,150], and, where sub-resolution porosity carries the flow, a resolution-limit caveat is given: for a fly-ash geopolymer imaged at 0.74 µm voxels, CT-based Stokes permeability came out two orders of magnitude above the MIP-based Katz–Thompson estimate, a gap the authors attributed to MIP rather than to CT [145], while sub-micron pores remain below CT resolution [21]. Crack metrics—volume, aperture width, orientation, surface area, and their evolution—treat cracks as a distinct void class, central to damage and self-healing studies [12,15,70,73–75,77,151–153]. Image-based finite-element or homogenization models built on CT geometries link pore structure to stiffness and strength [4,122,128,154]. These couplings are the strongest scientific argument for CT over indirect porosimetry: the geometry that enters the simulation is the geometry that exists.

4.6. Methodological Descriptors

Finally, two descriptors qualify the reliability of all the others: the REV status of the analyzed volume [4,78,79,99,100], and the segmentation approach with its sensitivity [32–34,38,93,94]. We treat them as first-class metrics deliberately: a porosity without its REV and segmentation context is a number without an uncertainty.

5. The Scale-Resolved Research Landscape

Figure 8 maps the distribution of the 140 application studies over voxel-size classes and material domains. This section walks through the five classes (Sections 5.1–5.5); Section 5.6 then turns to the aggregate patterns of metric usage, source venues and publication trends.

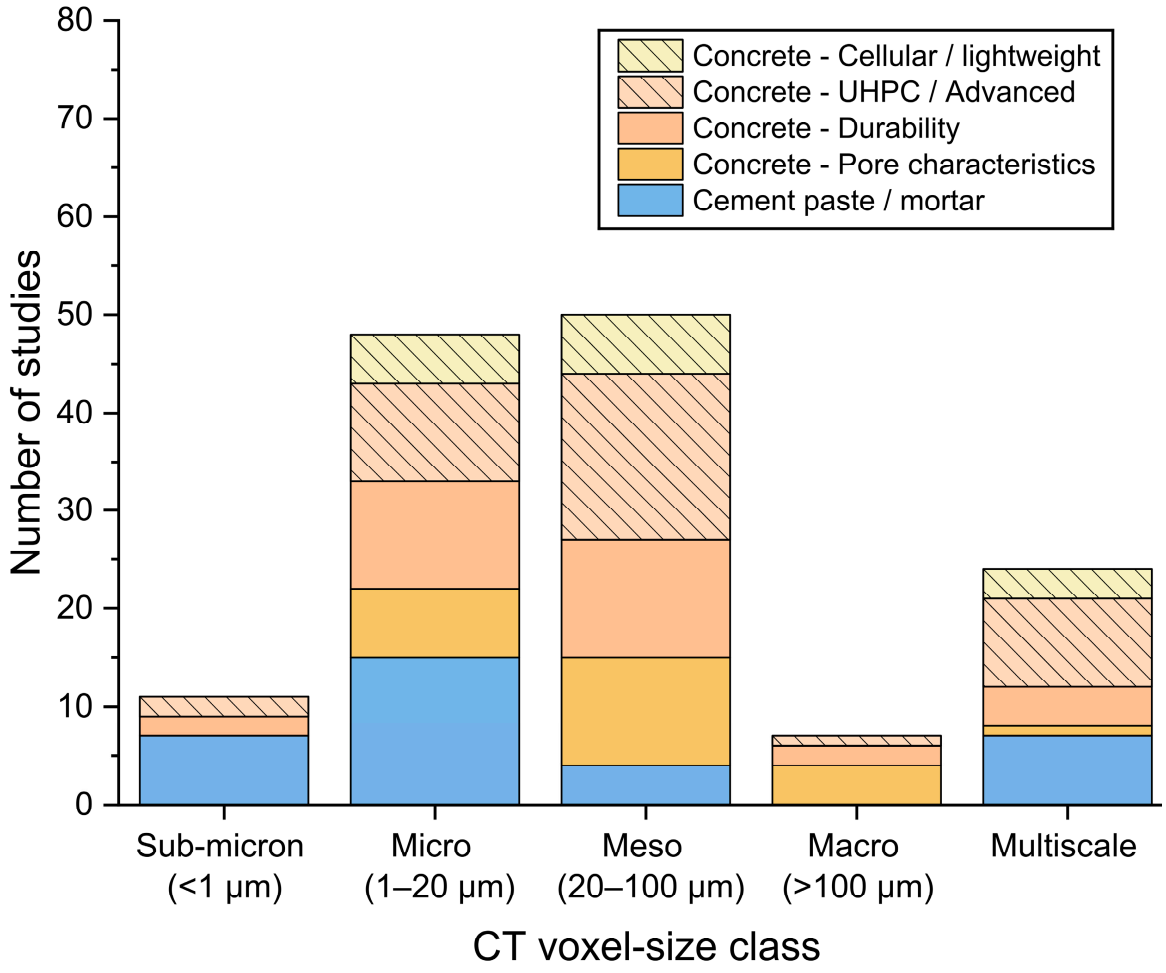

Figure 8. Distribution of 140 application-corpus records by assigned CT voxel-size class (sub-micron 11, micro 48, meso 50, macro 7, multiscale 24) and material domain (cement paste/mortar 33; concrete—pore characteristics 23, durability 31, UHPC/advanced systems 39, cellular/lightweight 14). Provisional assignments and review-category conventions are explained in Section 2.

5.1. Sub-Micron Class (Voxel < 1 µm)

Sub-micron-voxel tomography of cementitious materials remains rare (11 studies in the application corpus), despite the fact that most hydrate porosity lies below 1 µm. Nine concern cement paste—with seven coded to the paste/mortar domain (synchrotron monitoring of microstructure evolution during hydration [26,62], laboratory micro-CT cross-validated against Rietveld phase quantification at a single hydration age [65], tortuosity quantification in hardened paste [30], pore-structure characterization of leached and deteriorated paste [31,95], pore-network and water-uptake analysis of slag-blended pastes at 0.875 µm voxels [7], and two carbonation studies at 0.65 and 0.75 µm voxels coded to the durability domain [13,14]) and two concerning alkali-activated binders [145,155]. Figure 9 illustrates characteristic output of this class: sub-micrometer-voxel 3D pore maps with pores classified by size [7]. Even here, only the coarsest capillary porosity—features upward of roughly 2–3 µm—is resolved, and there is no gel porosity whatsoever; true nano-CT and ptychographic tomography (below ~150 nm resolution) reach finer populations in

paste fragments tens of micrometers across, but enter the corpus only within multiscale studies [19,53], at the price of fields of view far below any REV for transport properties and of severe specimen-preparation demands. The class consequently informs and calibrates models rather than characterizing materials in the engineering sense. The asymmetry between the physical importance of sub-micrometer porosity and its near-absence from the CT literature is the starkest instrumental asymmetry in the field [19,24,53].

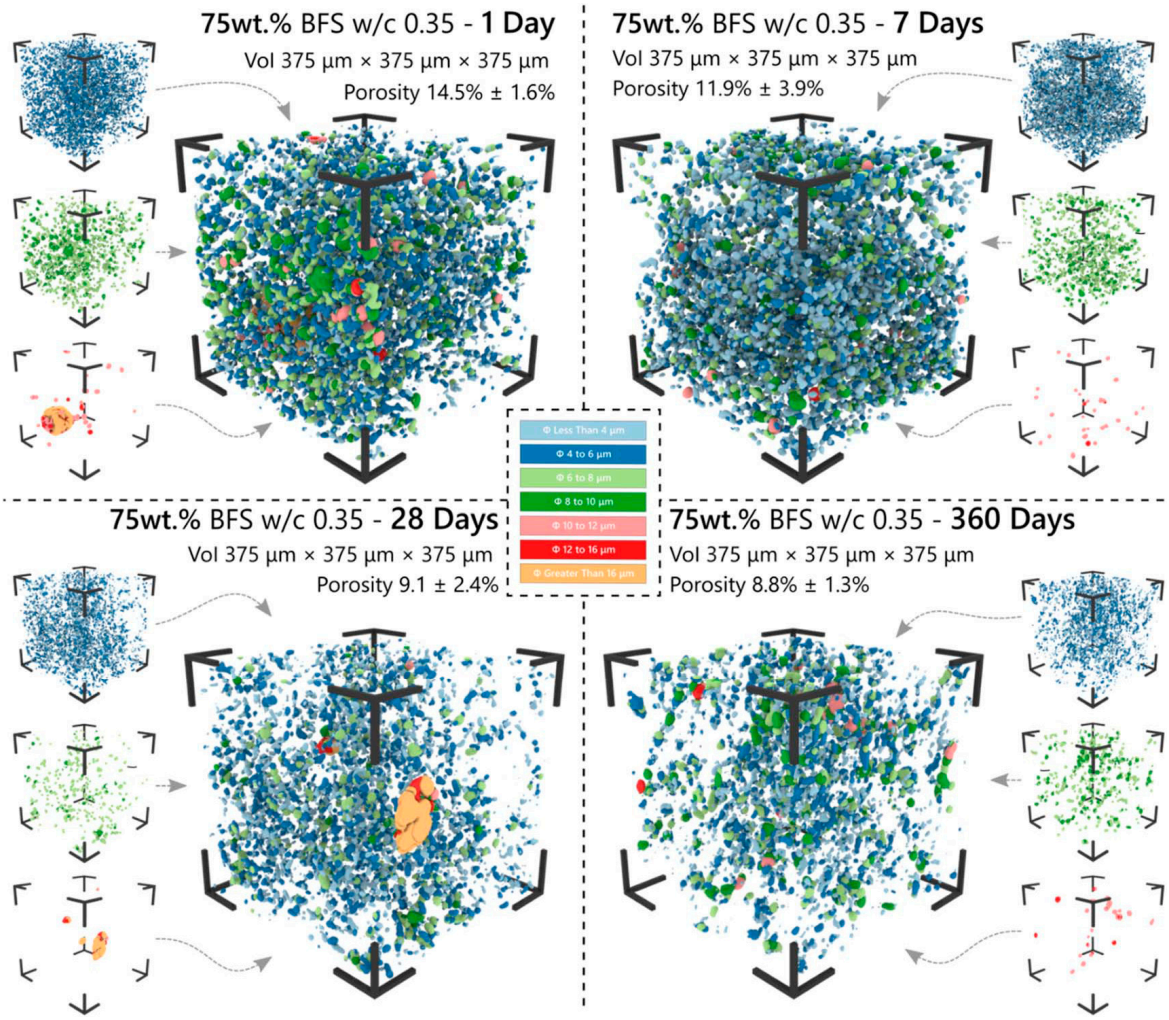

Figure 9. Sub-micron-class three-dimensional visualization of pore space in slag-blended pastes. Sub-micron-class (0.875 µm voxel) 3D visualization of the segmented pore space in 75 wt% slag-blended hardened cement paste at 1, 7, 28 and 360 days, with pores color-coded by size range. Reproduced from Vigor et al. [7], *RSC Advances*, open-access (CC BY 3.0).

5.2. Micro Class (1–20 µm)

The micro class accounts for 48 of 140 application studies, a similar share to the meso class (50/140). It is fine enough to detect entrained air, hollow-shell hydration voids, microcracks, interlayer voids and the coarsest capillary porosity, while accommodating paste and mortar specimens of several millimeters—a compromise that suits laboratory micro-CT perfectly. Canonical micro-class programs include hydration monitoring [55], paste–void spacing analysis [118,119], MIP benchmarking [22] and segmentation development, including a gradient-based phase method [56]; the pre/post-MIP comparison [23] and CT REV acquisition study [79] are categorized as multiscale. Their finest-voxel counterparts—synchrotron hydration monitoring [62], laboratory hydration quantification at 0.8 µm voxels [65] and

pore-structure analysis of deteriorated paste [95]—fall in the sub-micron class of Section 5.1. The base set of Table 5 (Section 8) is written with precisely this workhorse class in mind.

5.3. Meso Class (20–100 µm)

The meso class (50/140) is the scale of concrete as a composite: air-void systems, aggregate–paste interfaces, fibers and damage. CT air-void characterization at micro-to-meso voxels has matured into a practical laboratory alternative to ASTM C457 linear traverse, delivering spacing factors, void-size distributions and specific surface without polishing or operator fatigue [81,108,117,118], subject to the small-void resolution caveat discussed in Section 7.2. Damage studies span micro-to-meso voxels and track crack systems through freeze–thaw, corrosion and loading [9,11,70,71,156], and recycled-aggregate concretes are imaged at meso and fine-micro voxels to separate old mortar, new mortar, aggregate and porosity—a four-phase segmentation problem unique to the domain (Figure 10) [57,142,157,158]. Meso-class metric usage differs from the micro class in one respect (Figure 11): alongside porosity, PSD and spatial-distribution mapping, it hosts most of the corpus's anisotropy (5 of 6) and fractal-dimension (7 of 8) reporting, while topology remains thin. The binding constraint of the class is the undetected 10–50 µm small-void tail: meso-class air-void metrics should therefore travel with the minimum counted pore size of Table 5, and the standard-track ambition of Priority 6 hinges on stating it.

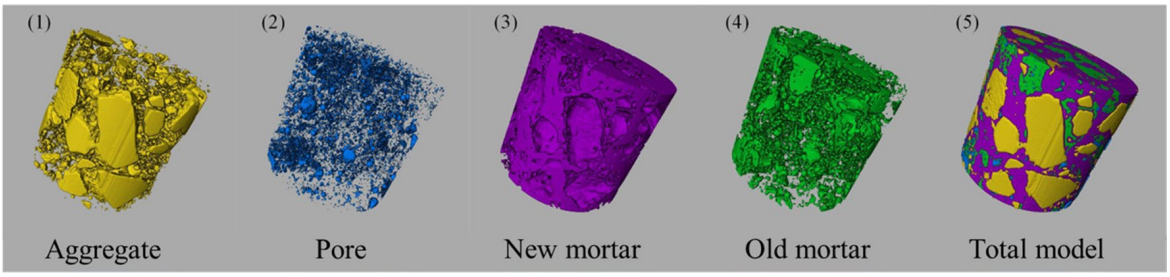

Figure 10. Meso-scale phase segmentation of recycled-aggregate concrete from micro-CT: aggregate, pores, new mortar, old mortar and the assembled model. Reproduced from Chen et al. [57], *International Journal of Concrete Structures and Materials*, open-access (CC BY 4.0).

5.4. Macro Class (Voxel > 100 µm)

Macro-class studies (7/140) scan large specimens—slabs, cores, piles and printed elements—at voxel sizes above 100 µm, resolving only voids and cracks upward of several hundred micrometers. The class is dominated by pervious concrete, whose functional macro-pores of millimeter size are fully resolved even at coarse voxels: four of the seven studies quantify pervious pore networks, connectivity, tortuosity and permeability on large specimens [59–61,150], and two further pervious-concrete studies fall in the meso class [5,149]. The remainder exploit large-volume coverage where spatial statistics outweigh resolution: freeze–thaw damage evolution in coal–gangue–aggregate concrete imaged by dual-helical scanning on an industrial CT system at 0.5 mm slice spacing [114], crack and pore evolution in paste exposed to elevated temperature [152], and bead-induced macroporosity in UHPC [159]. At such slice spacings, the achievable voxel size, not specimen penetration, is the binding constraint. The metric vocabulary of the class centers on porosity, size distribution, void distribution, connectivity and permeability prediction, and because these functional pores are fully resolved, it carries the widest per-study vocabulary of any class (4.6 metrics per study on average; Figure 11). The chief obligation of the class is therefore the base set of Table 5, so that its connectivity and permeability values are not pooled uncritically with micro-class ones.

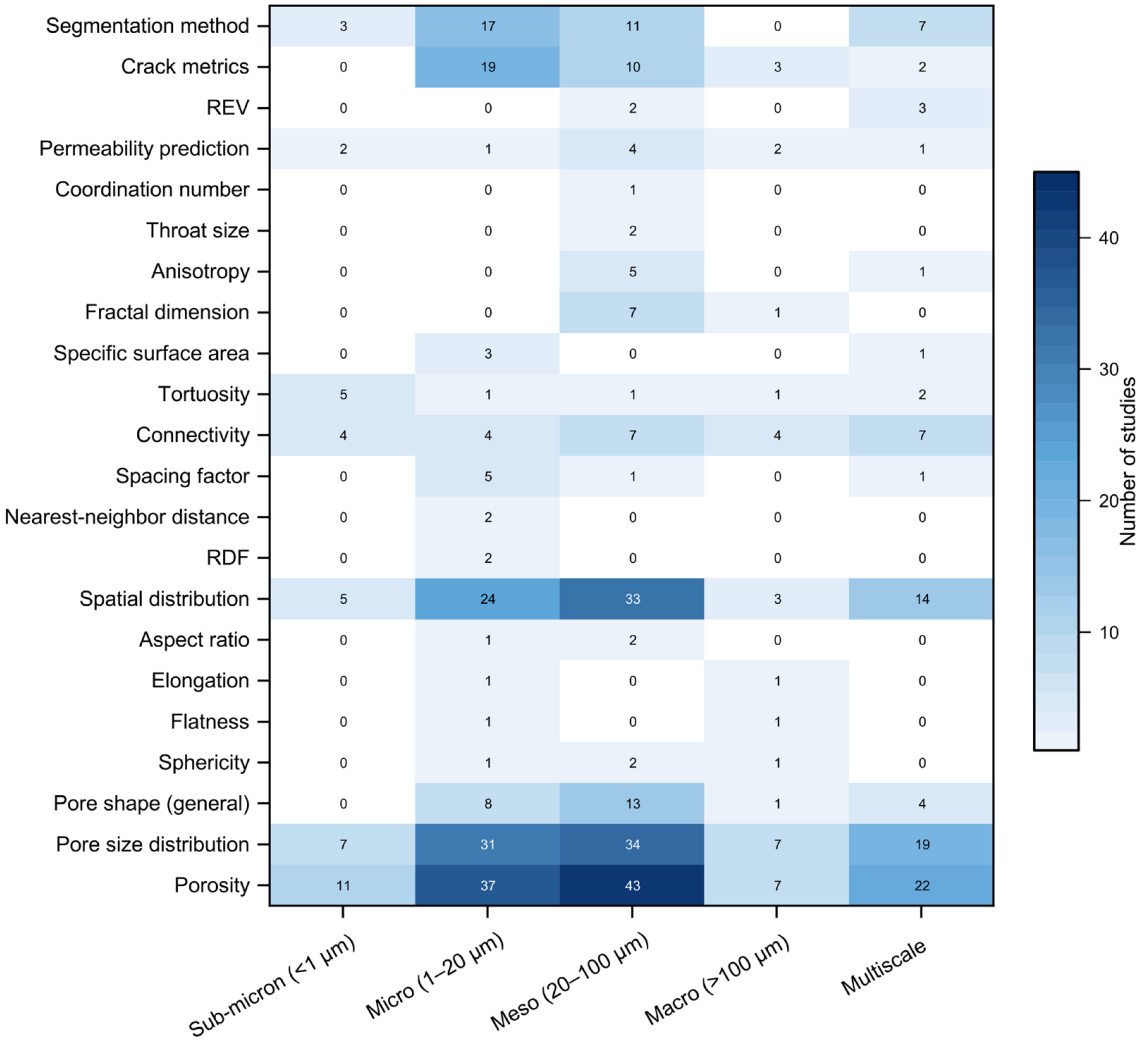

Figure 11. Metric usage frequency by voxel-size class: number of the 140 application-corpus studies reporting each metric of the Table 3 taxonomy, for each voxel-size class of Table 1.

5.5. Multiscale Studies

The multiscale category contains 24 of 140 records, including domain reviews and one provisional multi-technique record; it is therefore not a count of experimentally demonstrated multi-resolution CT. Experimental examples include paired, local/full-volume and resolution-sensitivity acquisitions [10,23,24,53,54,64,79,151,160], while domain reviews synthesize wider scale ranges [12,19–21,52]. The standard pattern is hierarchical: a coarse scan locates representative subregions, which are then re-scanned at finer voxel size—by physical subsampling, or by local (interior) tomography of the intact specimen, which avoids cutting at the cost of the truncation and gray-value artifacts noted in Section 3.1 [27–29]; porosity spectra are then concatenated across scales. The closest approximations in the corpus are same-specimen or same-mix acquisitions at two or three resolutions, whose resolution-conditioned porosities or pore-size distributions are compared explicitly [24,53,54,64,160]—including one lightweight-concrete study that concatenates air-void size distributions from a 55 µm whole-specimen scan and 9 µm scans of a core cut from it through a power-law bridge [160]. Formal fusion—registering scans of the same volume at different resolutions and reconciling their porosities into one audited spectrum—is not demonstrated by any application record reviewed here. Given that the resolution–REV dilemma (Section 3.4) is fundamental rather than instrumental, multiscale protocols are the only principled route to a complete pore description, and their scarcity is the field's most consequential method-

ological gap. They are also where the reporting rows of Table 5 matter most: without per-scale voxel sizes and registration accuracy, a concatenated pore spectrum cannot be audited (Priority 2).

5.6. Aggregate Patterns: Metric Families, Journals and Trends

Aggregated by family (Figure 12), amount/size metrics account for the largest share of study–metric pairs (222 of 489), followed by spatial arrangement (96)—driven largely by generic void-distribution mapping rather than formal spatial statistics—with the morphology (45), methodological (43), performance-linked (44) and topology (39) families each far behind. Within the morphology family, moreover, 26 of the 45 pairs are generic or qualitative shape reporting, leaving formal quantitative descriptors rarer still (19 pairs). Formal shape descriptors are strikingly rare: sphericity appears in four application studies [51,58,59,109], and flatness and elongation appear in two [1,59]; these tallies rise only to six and four when the two non-cementitious methodology sources that formalized the descriptors [132,133] are counted. The radial distribution function appears only twice [1,119]. Publication trends (Figure 13) show micro- and meso-class output accelerating sharply after 2018, coinciding with the arrival of 3D-printed concrete—which made anisotropic void fabric a mainstream concern [17,120,121]—and of accessible deep-learning segmentation [90,98]; the search-channel conditioning noted in Section 2 applies to these curves too, so the acceleration should be read against overall publication growth in the field rather than as a normalized rate. Sub-micron records remain few; the plotted counts alone do not establish whether instrumental barriers have changed.

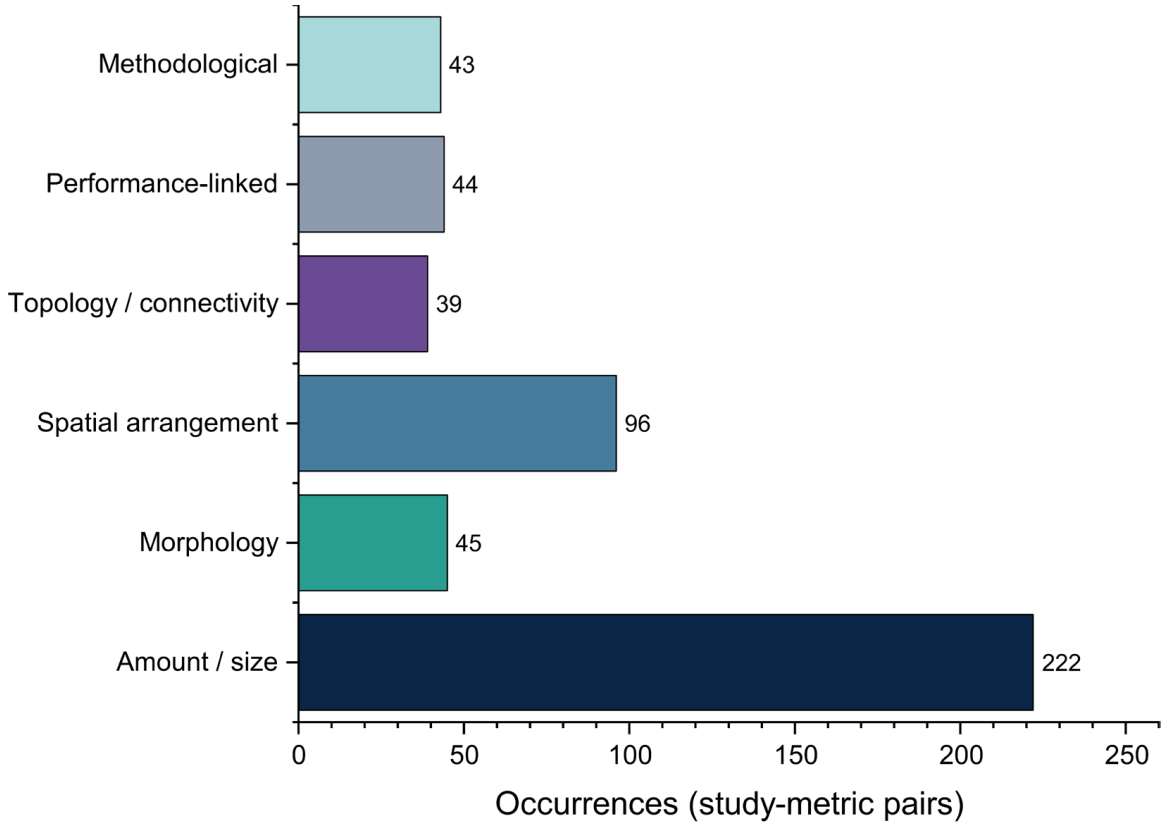

Figure 12. Usage frequency aggregated by metric family (study–metric pairs; application corpus, n = 140).

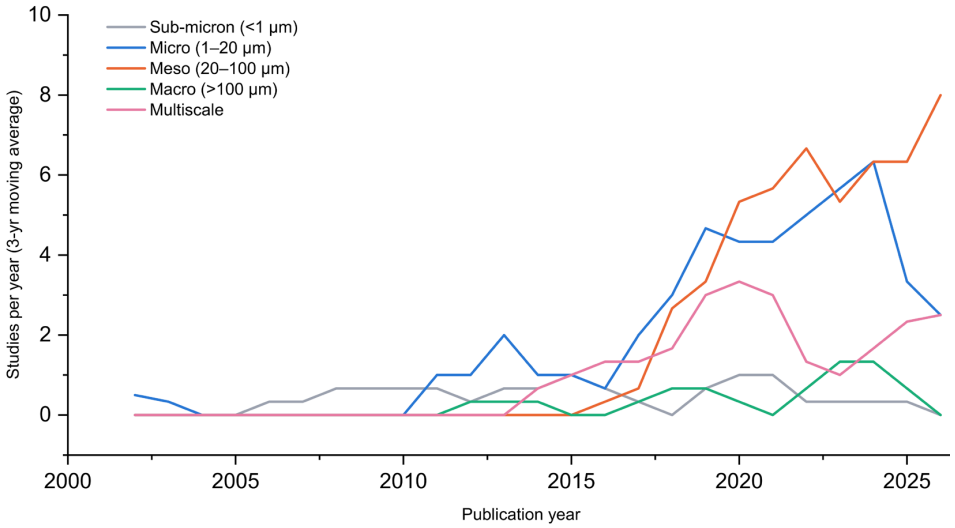

Figure 13. Publication trend by voxel-size class (3-year centered moving average; application corpus). The first (2002) and last (2026) points are means of the two available years only. The literature coverage extends through mid-2026; the final point is provisional.

The corpus concentrates in a handful of venues (Figure 14): *Construction and Building Materials* alone contributes about a quarter of the application studies (36/140), with *Cement and Concrete Research* (19), *Materials* (18), *Cement and Concrete Composites* (15) and *Journal of Building Engineering* (10) following—a distribution that mirrors the field's applied center of gravity and its dependence on a few flagship journals. Co-occurrence analysis (Figure 15) shows that amount/size metrics accompany nearly every other family, whereas morphology and topology co-occur with each other far less often than either does with porosity: studies tend to add one 'higher-order' metric family to the porosity baseline rather than characterizing shape, arrangement and topology jointly. Truly comprehensive characterizations—four or more families in one study—number 14 of 140 and span the corpus's material domains, including durability, paste/mortar and 3D-printing studies as well as foamed- and pervious-concrete work [54,59,95,111,114,128]. These aggregate patterns set up the question Section 6 answers: Why can the numbers behind them not yet be compared at face value?

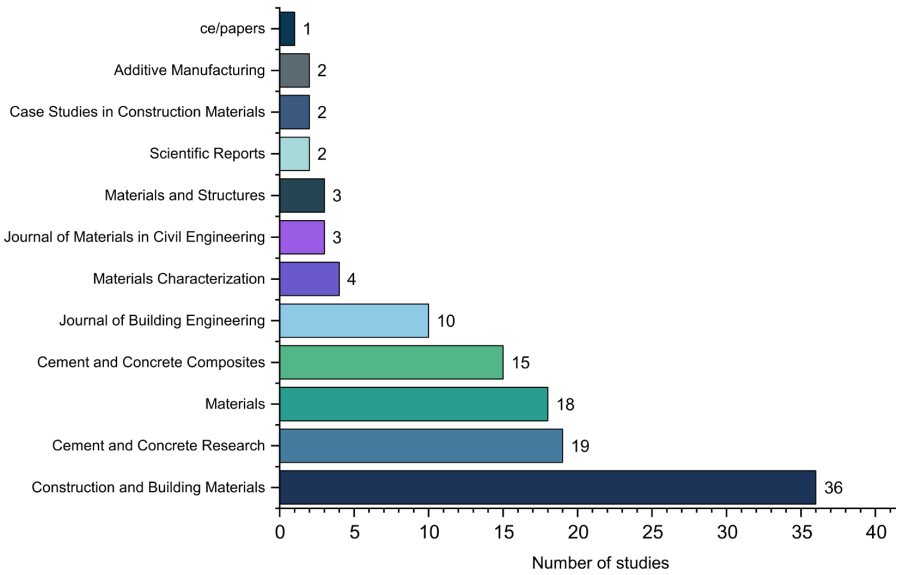

Figure 14. Source journals of the application corpus (top 12 by number of studies). The twelfth position (n = 1) is one of several tied single-study journals.

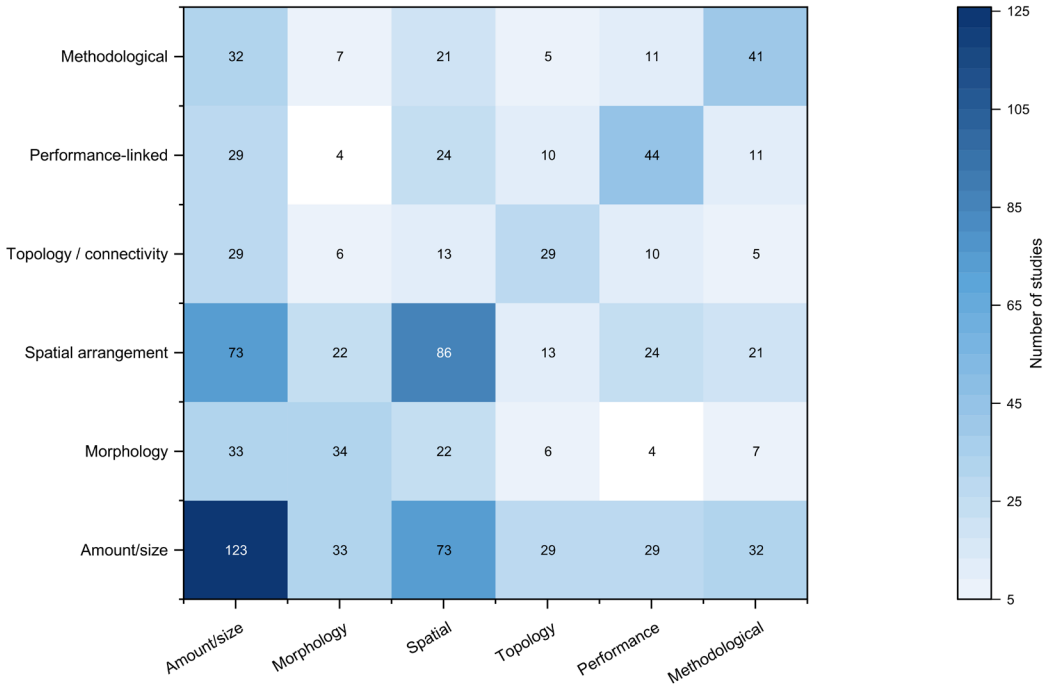

Figure 15. Co-occurrence of metric families within single application-corpus studies (diagonal: total studies reporting each family).

6. Cross-Scale Discrepancies and Peculiarities

Comparing results across the corpus exposes systematic incompatibilities that are structural—rooted in physics and workflow—rather than accidental. Before listing them, it is useful to name what each incompatibility corrupts. Every CT-derived pore metric is conditioned on three separable elements: the observation window (the imaged volume and its relation to the REV), the resolved population (the subset of pores the voxel size and segmentation actually capture), and the descriptor definition (the mathematical convention by which the captured pores are summarized). Cross-study disagreement can enter through any of the three, and remedies differ accordingly: window problems call for larger or registered volumes, population problems for resolution and segmentation reporting, and descriptor problems for convention standardization. We identify seven discrepancies and structural gaps below and tag each with the element(s) it involves: items (1) and (2) are population- and window-driven respectively; item (3) is population-driven through processing; item (4) couples a population-driven resolution bias to a descriptor-level coverage gap; items (5) and (6) are descriptor-driven—the former as a coverage gap, the latter as a convention problem; and item (7) shows the three interacting as new processes create new void classes. Figure 1b depicts the three elements; the mapping of each discrepancy onto the element(s) it involves is given in Section 8.

Ranked jointly by the magnitude of the distortions documented in the corpus and by whether they can be corrected after publication, these seven discrepancies are not equally damaging. Resolution conditioning (items 1 and 2) dominates: it biases paste porosities by factors of two or more, no post hoc correction can recover pores that were never resolved, and—on the evidence currently in the corpus—it is the only discrepancy that better reporting alone cannot repair. Segmentation choice (item 3) can rival it in magnitude in the worst case, but differs decisively in correctability: its sensitivity can be quantified and reported at publication time. The descriptor conventions implicated in items 4 and 6 (axis and shape conventions, the τ-versus-τ^2 ambiguity of Section 4.4, terminology) produce factor-scale confusion between studies, yet vanish once conventions are stated; the coverage

gaps of items 4, 5 and 7—under-used shape, spatial and new-void-class descriptors—call for adoption rather than convention. In this ranking, the instrumental starvation of the submicron class (Section 5.1) and the scarcity of multiscale studies (Section 5.5) are the symptom and the remedy of a single root—resolution conditioning—rather than independent gaps.

(1) Resolution-conditioned porosity: CT porosity is not a material constant but a function of voxel size: coarsening voxel size silently transfers pores from 'resolved' to 'invisible' [24,64]. Comparative studies against MIP [22–24] report CT porosities for paste lower by factors of two or more [22]; the two techniques see complementary populations rather than the same one—MIP registers intrusion throats but not the air-void chambers that CT resolves [23]—so concordance for entrained air is established against ASTM C457 stereology rather than against MIP (Section 7.2) [81,108,118]. Sub-resolution porosity can be partially recovered from grayscale statistics [63] or inferred stoichiometrically from the segmented unhydrated-cement fraction via Powers' hydration model [91], but few applied studies attempt either. Any cross-study comparison of 'porosity' that ignores acquisition scale is therefore confounded by construction [54,63] (Table 5, amount/size row). The intrusion–extrusion hysteresis that arises from the ink-bottle effect is illustrated in Figure 16 [25].

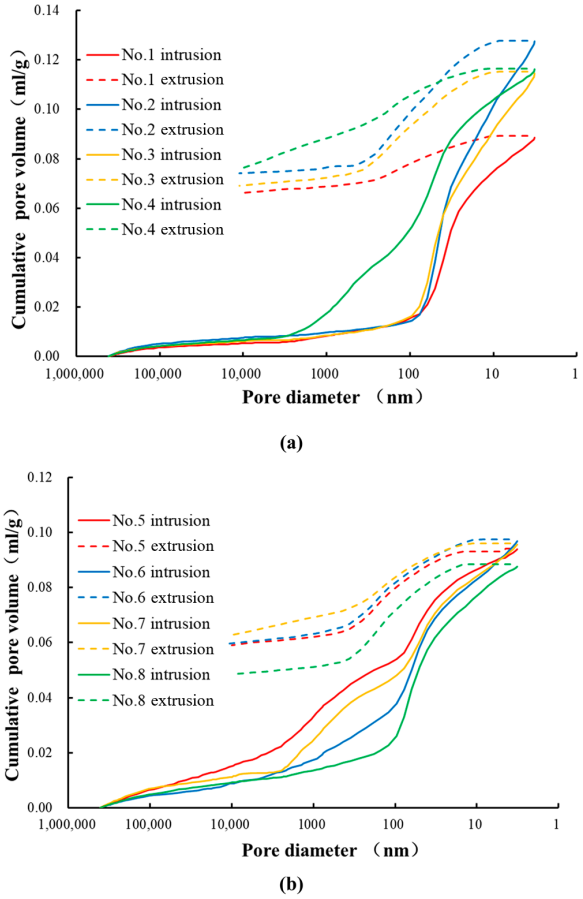

Figure 16. Cumulative mercury intrusion–extrusion curves of cement-based materials: the pronounced hysteresis and entrapped mercury reflect the ink-bottle effect, a principal reason CT-derived and MIP pore-size distributions diverge (total-porosity gaps are driven chiefly by resolution truncation; Section 6, item 1) ((**a**) mixes No. 1–4 and (**b**) mixes No. 5–8 of the source study). Adapted from Zhu et al. [25], *Scientific Reports*, open-access (CC BY 4.0); the legend labels have been corrected from the original's "etrusion" to "extrusion", with no other change.

(2) The REV–resolution dilemma: The volumes required for representative connectivity or tortuosity exceed what can be imaged at the resolution required to segment capillary pores—meaning that some frequently cited micro-scale topology values are, strictly speaking, not representative of the material [54,78,79,100]. The dilemma is geometric, not instrumental: doubling detector pixels relaxes it only by a factor of two, while the CT-relevant pore-size span covers about four orders of magnitude (of the roughly six that the full nanometer-to-millimeter pore spectrum occupies; Section 1). Multi-resolution imaging with explicit cross-resolution comparison is the principled response [19,24,53], with registered fusion as its target end state, but reporting REV status alongside every topological metric would already remove most of the silent damage.

(3) Segmentation variance that is comparable to material effects: Comparative evaluations show inter-method spreads on identical images—demonstrated directly as criterion-dependent void-ratio divergence [32] and as relative phase-quantification errors of tens of percent [33], and equally on soils and carbonates [34,93]—of the same order as the differences between water–cement ratios or curing regimes that applied studies aim to detect; no cementitious study in the corpus has yet quantified the two side by side (Table 2 lists the reported sensitivities). The corpus nevertheless rarely reports segmentation sensitivity, and only a minority of applied studies state their thresholding rationale in reproducible detail. Deep-learning segmentation does not dissolve the problem; it relocates it into training-data selection and annotation quality [35,90,97,98]. This is the field's largest invisible reproducibility debt (Table 5, base set; Priority 1).

(4) Shape metrics are resolution-biased and under-used: A pore spanning a few voxels cannot yield a meaningful sphericity or elongation; commonly reported safe thresholds for shape analysis range from roughly 10 to 30 voxel diameters depending on the metric and the surface estimator (Section 4.2). This partly explains why shape analysis concentrates in materials with large voids—foamed, pervious and 3D-printed concretes [2,17,59]—and why it is nearly absent for capillary porosity. Yet even where voids are large, most studies stop at qualitative 'rounded versus irregular' commentary rather than computing principal-axis descriptors; this is a missed opportunity given the mechanical relevance of flat and elongated voids as stress concentrators [2,3,121] and the availability of formalized descriptors for them [132,133] (Table 5, morphology row; Priority 5).

(5) Spatial statistics are almost absent: Beyond the air-void spacing factor inherited from freeze–thaw practice [81,108,117,118], formal spatial descriptors of CT-derived pore centroids—pair correlation/RDF, nearest-neighbor distributions, and clustering indices—are essentially unused [118,119], even though interlayer-void alignment in 3D printing, void clustering in ITZ regions, and depth-graded porosity under degradation are inherently spatial phenomena [18,71,120,141,161]. Two-point correlation functions are well established in cement microstructure modeling and stochastic reconstruction, so the claim is deliberately narrow: it is the application of such statistics to CT-measured pore positions that is missing. The tools are mature in particle physics and spatial statistics and port directly; their absence from CT pore analysis appears cultural rather than technical (Table 5, spatial-arrangement row; Priority 4).

(6) Terminology drifts across scales and domains: 'Pore', 'void', 'air void', 'defect' and 'crack' partition the void space differently in different subcommunities: durability studies treat cracks as damage to be quantified [12,152], 3D-printing studies treat interlayer voids as a process signature [17,161,162], air-entrainment studies treat voids as designed microstructure [81,108,117], and pervious-concrete studies treat

connected macro-pores as the functional phase [59,60]. Identical geometric objects receive different names, different metrics and different fates in meta-analysis. Cross-scale synthesis requires an explicit, geometry-based void ontology rather than domain-specific jargon.

(7) New processes create new void classes—and new metrics: 3D-printed cementitious materials introduced systematically anisotropic, oriented interlayer voids with little precedent in conventionally cast concrete; within five years, orientation and anisotropy metrics moved from exotic to standard in that subdomain [17,18,110,120,121]. The episode is consistent with metric vocabularies responding to processing innovation—and suggests, though a bibliometric trend cannot prove, that the under-use of spatial and shape statistics in cast concrete reflects perceived need rather than any fundamental obstacle. Figure 17 shows a representative advanced-material pore structure (a geopolymer foam) of the kind whose characterization requires such extended metrics; the oriented interlayer-void fabrics of printed elements [17,18,120] make the same case for anisotropy descriptors.

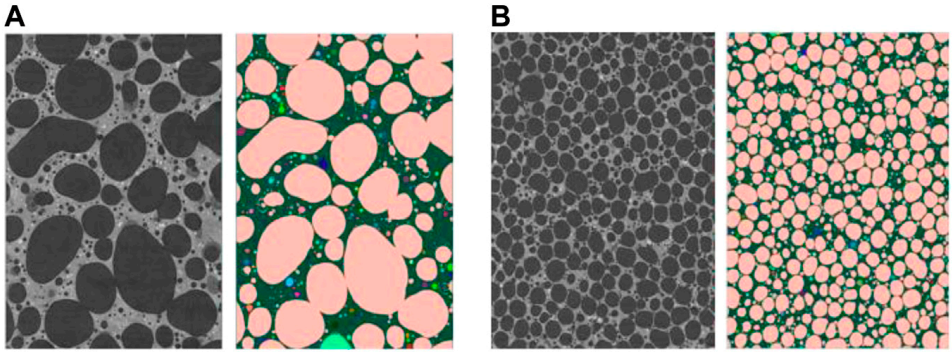

Figure 17. Percolated pore network of a geopolymer foam. Vertical CT cross-sections (**left** of each pair) and segmented pore clusters (**right**) of geopolymer foams prepared with (**A**) AER5 and (**B**) CTAB surfactants at the same blowing-agent content; pink marks the percolating pore cluster and other colors mark the isolated clusters (voxel size 10 μm in **A**, 5 μm in **B**), illustrating the large, partly coalesced void systems characteristic of advanced cementitious materials. Reproduced from Petlitckaia et al. [131], *Frontiers in Chemistry*, open-access (CC BY 4.0).

7. Synthesis by Material Domain

7.1. Cement Paste and Mortar

The paste-and-mortar domain (33 studies) is where the field's methods are made: essentially every image-analysis technique later used on concrete—segmentation, REV analysis, benchmarking against MIP, spatial statistics—is validated here first [19,20,26]. What the domain has learned is foundational, even where negative: at accessible voxel sizes, most capillary and all gel porosity is invisible, so paste-scale CT porosities are lower bounds whose meaning depends jointly on voxel size and segmentation (Section 6, items 1–3). Its distinctive positive capability is time resolution—hydration, water uptake and microstructure development followed non-destructively in the same specimen [26,62]—and porosity mapping across mixtures, additions and curing regimes [163–167] now supports mixture-level conclusions that 2D microscopy could not deliver. Those capabilities keep their value only as long as the base-set metadata of Table 5 travel with them. Nano-reinforced mortar characterization provides a further paste/mortar example [168].

7.2. Concrete at the Meso and Macro Scales

The concrete domain (23) delivers the corpus's most direct engineering payoffs, and its central finding is that CT can measure, in three dimensions and without polishing,

the void parameters that standards currently obtain stereologically. CT air-void analysis reproduces spacing factors, void-size distributions and specific surface with favorable single-laboratory repeatability relative to ASTM C457 linear traverse [81,108,118]. The case for replacement is nevertheless not yet closed, for a technical as well as an institutional reason: entrained-air systems extend down to ~10–50 µm voids, a small-void tail that dominates void frequency, and meso-class voxels (20–100 µm) cannot detect it—truncating the distribution and biasing specific surface and the computed spacing factor toward coarse-void values; no inter-laboratory validation or standards-body adoption yet exists. Pervious-concrete studies, concentrated in the macro and meso classes, establish quantitative links from connected macro-pore networks to measured and simulated permeability [5,59–61,150], and extend to in-service functional degradation through CT-quantified clogging of the pervious pore network [169,170]. Pore-structure studies of fiber-reinforced concretes, foams and mortars [171–173] are counted in the corpus, whereas a CT fiber-spacing study [174] supplies only complementary context—fiber-only descriptors are excluded from pore-frequency counts. In-situ load-stage imaging ties damage evolution to meso-structure [68,70,104]; ex-situ before/after scanning of fiber pull-out specimens quantifies pull-out-induced changes in pore volume along the fiber axis and is counted in the corpus [175], whereas post-compression crack-path imaging of pore-engineered concrete [176] supplies only a complementary, non-time-resolved context without contributing pore metrics. Comprehensive multi-method characterizations that couple CT pore metrics, including spatial-heterogeneity descriptors such as lacunarity, with mechanical testing on the same concretes are emerging (Figure 18) [177]. The checklist rows most binding in this domain are the minimum counted void size and the specific-surface estimator of Table 5, prerequisites for the inter-laboratory validation that Priority 6 calls for.

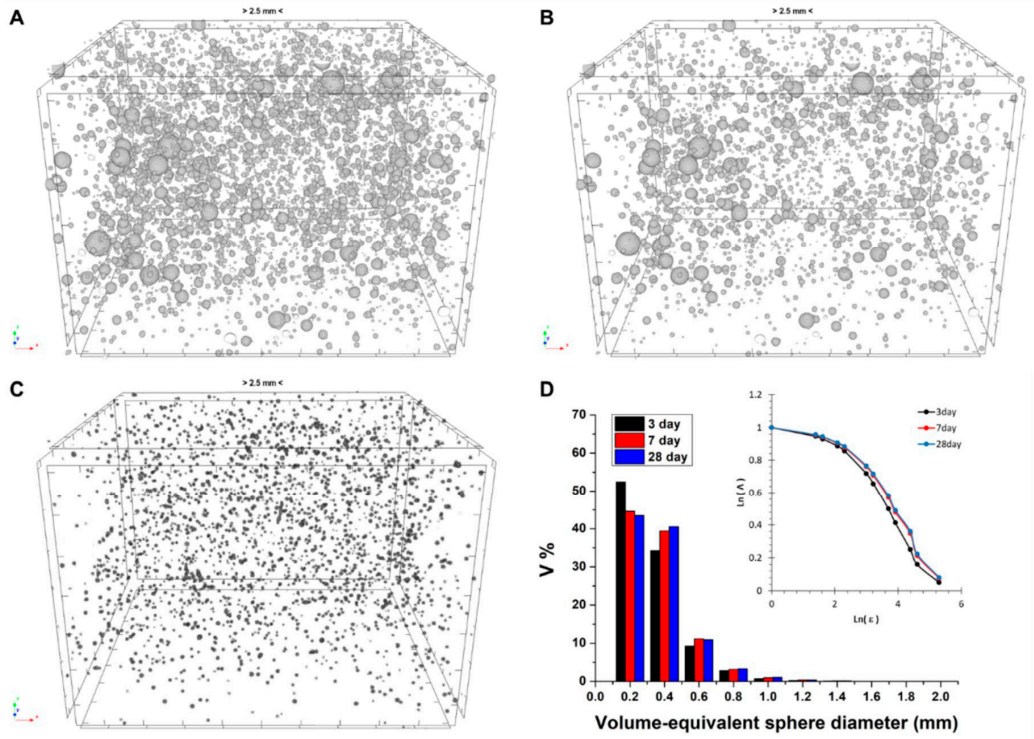

Figure 18. Micro-CT pore renderings and equivalent-sphere diameter distributions of concrete. (**A**,**B**) Micro-CT 3D renderings of the segmented closed-pore space of a concrete cube after 3 and 28 days of curing and (**C**) the pores that disappeared between 3 and 28 days; (**D**) the corresponding volume-equivalent sphere diameter distributions at 3, 7 and 28 days, with the lacunarity curve (ln Λ versus ln ε) inset, from a comprehensive multi-method characterization. Reproduced from Vásárhelyi et al. [177], *Materials and Structures*, open-access (CC BY 4.0).

7.3. Durability and Degradation

The durability domain (31) exploits the one capability no other pore-characterization technique offers—longitudinal, non-destructive re-measurement of the same specimen through degradation—and its collective finding is that degradation mechanisms are better discriminated by where and how the pore system changes than by how much total porosity changes. Specimens are scanned before and after, or repeatedly through, freeze–thaw cycling [9,71,72,115,117], sulfate exposure [16,141], corrosion-induced cracking [11,151,156, 178,179] (reviewed in [12]), elevated temperature [66], alkali–silica reaction [15,180–182] and self-healing [73–77]; related studies compare separately exposed specimens, each scanned at a single exposure state [13,14,152], or scan only the pristine pore structure and relate it to the freeze–thaw performance of companion specimens from the same batch [183]. The characteristic outputs are differential: pore-structure evolution, crack initiation and growth, and healing-product infill quantified exposure step by exposure step. Recycled-aggregate concrete adds its four-phase segmentation problem (old mortar, new mortar, aggregate, porosity) and the associated double-ITZ porosity [123,157,158]. Methodologically, this domain pushes registration (aligning repeat scans) and change detection—capabilities largely absent elsewhere in the corpus. A representative durability workflow is the CT-based phase separation of a steam-cured concrete into pores, mortar and aggregate across a freeze–thaw campaign [71]. Because every differential claim rests on aligned repeat scans, registration method and accuracy belong beside voxel size in the base set of Table 5; their routine omission is the domain-specific face of Priority 3.

7.4. Advanced Cementitious Systems

The advanced-materials block (39) is the fastest-growing, and it illustrates how metric vocabularies follow processing innovation: each new material class has forced a new descriptor into routine use. Alkali-activated and geopolymer systems show pore structures—and pore-formation mechanisms—distinct from Portland systems, with tortuosity and network topology as early flagship metrics [116,131,145,155,184–186]. 3D-printed cementitious materials contribute the interlayer-void problem, its anisotropy metrics and the coupling between printing parameters, interlayer bonding and pore structure [17,18,110,111,120,121,161,162,187–192]; UHPC studies couple fiber orientation with void fabric [137,159], while CT fiber-orientation methodology itself has been developed largely outside the pore-metric corpus [136,139,140,193,194]; engineered cementitious composites add fiber–pore–crack interactions [69,90,195–197]; bio-based concretes (hemp) bring extreme, multi-modal porosity [50,124,198]. Because these materials lack decades of empirical characterization, CT is often their primary microstructural instrument rather than a complement—which makes the methodological hygiene issues of Section 6 disproportionately consequential here. For materials with no legacy characterization to fall back on, base-set compliance with Table 5 is not hygiene but the primary evidence base.

7.5. Cellular and Lightweight Concretes

Cellular and lightweight concretes (14) show what CT delivers when the pore population of interest is fully resolved: bubbles above roughly 0.3 mm are quantifiable at meso voxels, while the finer bubble tail drives part of the domain to micro-class or multi-scale imaging, and the domain consequently reaches quantitative structure–property links that paste-scale work cannot. Studies link bubble-size distribution, shape and connectivity to density, strength, permeability and thermal performance [2,6,64,128,199–202], with fresh-state foam stability and bubble coalescence as recurring explanations for irregular or interconnected pores [2,154,200]; earlier CT transport work on porous bricks [203] and pore-forming studies of sintered lightweight aggregate [204] supply methodological context. Its

large, well-resolved voids make the domain a natural host for shape analysis, including aspect ratio [2], alongside a porosity-homogeneity study [129]. Its fully resolved voids also make the domain the natural proving ground for the standardized shape reporting of Priority 5.

7.6. The Cross-Cutting Methodological Toolbox

The methodological and contextual reference set (56 references, inventoried separately from the application corpus; Section 2) supplies the shared instruments applied throughout cementitious CT work: general CT reviews [27–29,80], voxel-size sensitivity analysis [101], thresholding and segmentation comparisons [32–34,38,82–84,86–89,93,94,97,205], phase retrieval [102], pore-network extraction algorithms [36,37,39,96,146–148], REV theory [99,100], shape formalism [132,133], fractal analysis [134,135], tortuosity definition and computation [107,125–127], spatial point-pattern statistics [143], sub-resolution porosity estimation [63], deep-learning image-analysis reviews [92,98], and open software [105,106,206]. Notably, a large fraction of this toolbox originated in geoscience and biomedical imaging and was adopted by the cement community with little modification; this was efficient, but led to their importing assumptions (about phase contrast, pore geometry and typical size distributions) that are not always re-validated for cementitious microstructures. Cement-specific method validation—thresholding comparisons on cementitious specimens [32,33], CT REV analysis and complementary microscopy/modeling of cementitious volumes [78,79], voxel-size sensitivity analysis on alkali-activated slag paste [54]—remains the exception rather than the rule, and expanding it is itself a research direction (Priority 1).

8. Research Gaps and Outlook

Seven priorities emerge from the synthesis; they are ordered by tractability rather than by the damage ranking above, since the largest distortions are not the quickest to remove. (1) Segmentation benchmarks: the field needs public, expert-annotated cementitious CT datasets against which thresholding and learning-based methods can be scored; without them, segmentation-induced variance (Section 6, item 3) remains unquantifiable [32,33,86,97,98]. (2) Scale-bridging protocols: registered nano-to-meso imaging of the same specimen, with explicit rules for merging resolution-conditioned porosities into a single spectrum [19,24,53,54]. (3) Routine uncertainty reporting: every CT-derived metric should carry its voxel size, analyzed volume, REV status and segmentation sensitivity—the minimal metadata for meta-analysis [32,33,78,100]; Table 5 operationalizes this as a metric-conditional checklist keyed to the taxonomy of Section 4. (4) Adoption of spatial statistics: RDF, nearest-neighbor and clustering descriptors should become routine outputs, particularly for 3D-printed and air-entrained systems where arrangement, not amount, controls performance [118–120]. (5) Standardized shape reporting: principal-axis sphericity, flatness and elongation with stated minimum-voxel thresholds, replacing qualitative shape commentary [59,132,133]—noting, for transparency, that the few application-corpus exemplars of Priorities 4 and 5 include the corresponding author's prior study [1], and that the recommendation rests on the mechanistic arguments of Sections 4.2 and 4.3 rather than on that study. (6) Standard-track air-void analysis: formalizing CT air-void characterization as an alternative to linear traverse—for which single-laboratory evidence is encouraging, but inter-laboratory round-robin validation and explicit minimum-voxel-size requirements for unbiased small-void statistics must be established first (Section 7.2) [81,108,118]. (7) Physics-aware machine learning: segmentation and super-resolution models that ingest grayscale physics (partial volume, sub-resolution porosity) rather than treating CT volumes as generic images [35,63,91,92,98].

Behind all seven priorities stands a single geometric contradiction, encountered repeatedly in this review (Sections 3.4 and 6, item 2) and worth naming in full: representativeness and resolution are a zero-sum game. The volume a metric needs in order to represent the material and the voxel size it needs in order to resolve the pores that control it cannot, for capillary-scale quantities, be purchased in the same scan—and the constraint is geometric rather than instrumental, relaxed only linearly by better detectors while the pore spectrum spans orders of magnitude. Two responses exist today. The first—single-scale imaging accompanied by the metric-conditional reporting of Table 5—is available to every laboratory immediately, but it is honest bookkeeping rather than a solution: it makes the conditioning visible without removing it. The second—multiscale acquisition culminating in registered fusion—is the only principled resolution of the dilemma, yet 24 of 140 records are coded multiscale, including reviews and a provisional assignment, while the same-specimen or same-mix comparisons of resolution-conditioned porosity or pore-size distribution identified here number only five and none registers the volumes [24,53,54,64,160] (Section 5.5). The distinction matters because the segmentation debt of Section 6 (item 3) can be repaid by reporting, whereas the REV–resolution dilemma cannot. The authors therefore regard Table 5 as a minimum acceptable floor rather than a target, and propose that registered multiscale acquisition become the default expectation behind any connectivity or tortuosity claim made at micro-class voxels. Neither step requires instruments based on new physical principles, although sub-micron, phase-contrast and in situ CT and registered multi-resolution acquisition may require facilities beyond a standard laboratory (Section 5.5). Figure 19 maps the seven discrepancies onto the priorities through the three conditioning elements.

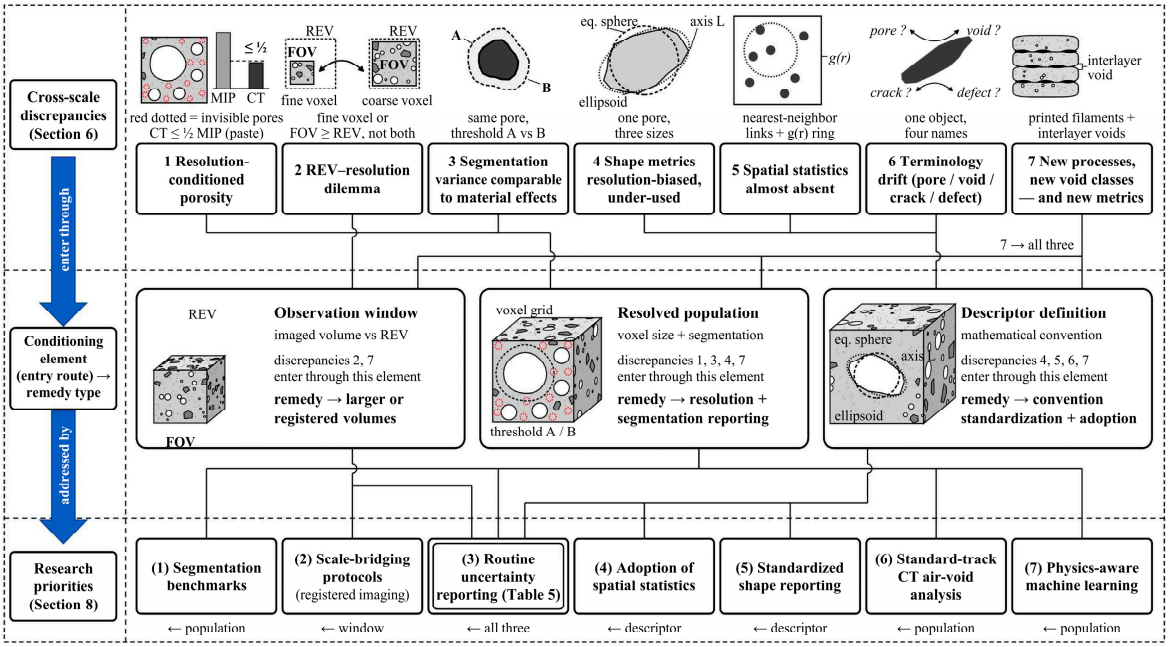

Figure 19. Synthesis of the review: the seven cross-scale discrepancies of Section 6 (**top**), the conditioning element through which each enters—observation window (items 2 and 7), resolved population (1, 3, 4, 7) and descriptor definition (4, 5, 6, 7)— with the remedy type (**middle**), and the seven research priorities of Section 8 (**bottom**), each linked to the element it addresses. Priority 3 anchors the metric-conditional minimum-reporting checklist of Table 5.

Table 5. Metric-conditional minimum reporting checklist for CT pore analysis of cementitious materials. Each row lists the metadata without which that metric family cannot be compared across studies.

Metric Family	Minimum Metadata to Report	Why It Is Required
All metrics (base set)	Voxel size; true spatial resolution estimate (if unmeasured, state 2–3× voxel size; Section 3.1); specimen and analyzed-volume dimensions; scanner type and energy; reconstruction and filtering steps; segmentation method with parameter values; specimen moisture/saturation state and drying protocol (age at scan recommended); REV status of the analyzed volume relative to the metric reported; segmentation-sensitivity estimate, or an explicit statement that none was performed; for repeat-scan and multiscale studies, registration method and accuracy	Every downstream number is conditioned on these acquisition and processing choices
Amount/size	PSD definition (discrete equivalent diameter vs. continuous local thickness vs. granulometry); minimum counted pore size in voxels; sub-resolution handling (grayscale-based sub-voxel estimation [63] or explicit truncation)	The three PSD definitions are not interchangeable; counting thresholds shift porosity and PSD tails
Morphology	Shape convention (e.g., S/I, I/L axes convention); surface estimator (voxel-face vs. meshed); minimum pore size in voxels for shape evaluation (recommended $\geq$ 10–30 voxels depending on the metric; Section 4.2)	Shape values are convention- and estimator-dependent and meaningless for few-voxel pores
Spatial arrangement	Reference structure (centroids vs. surfaces); edge-correction method (e.g., Ripley's corrections [143]); window size relative to the correlation length; for spacing factor, whether the Powers spacing factor ($\bar{L}$) or a direct 3D proximity distribution is reported	Point statistics are biased by edges and small windows; $\bar{L}$ and direct distributions are different quantities
Topology/connectivity	Connectivity definition (percolating fraction, Euler density, or beta-0); tortuosity type (geometric, hydraulic, diffusive, electrical) and τ vs. τ^2 convention; network-extraction algorithm and parameters; REV status of the analyzed volume	Topological quantities are the most definition- and algorithm-sensitive family in the corpus
Performance-linked	Simulation physics and boundary conditions; domain size vs. REV; validation against measured transport or mechanical data where available	Image-based predictions inherit all upstream conditioning plus solver assumptions

Beyond these methodological priorities, two structural shifts would compound their value. First, data sharing: raw and segmented cementitious CT volumes are large but not prohibitively so, and public repositories of even a few dozen well-documented volumes would enable the benchmarking, method comparison and meta-analysis that the printed literature cannot support. Second, closing the loop with design: the emerging couplings between imaged pore structure and simulated performance (Section 4.5) point toward pore-structure specifications—target spacing, connectivity or anisotropy values—entering mixture and process design, particularly for 3D printing, where the void system is a controllable process outcome rather than an accident of compaction [18,120,121].

X-ray CT complements rather than replaces the established pore-characterization techniques, and the framework proposed here is a CT-conditioned one. Gel and fine capillary porosity lies one to three orders of magnitude below the quantification limit of even sub-micron-voxel CT and remains the domain of gas adsorption, mercury intrusion porosimetry, NMR relaxometry and electron microscopy of polished sections (Table 4, Figure 2b) [22–25]. The productive configuration is correlative: CT supplies the three-dimensional connectivity, arrangement and morphology of the resolved population in an intact specimen, while intrusion-, sorption- and section-based methods supply the sub-resolution size distribution and specific surface [22,24,66]; the metric-conditional reporting of Table 5 is what allows the two populations to be combined rather than conflated.

9. Conclusions

This review classified 140 X-ray CT pore-analysis studies of cementitious materials by voxel-size class and by the pore metrics they report, and inventoried the discrepancies that arise when their results are compared across scales. The principal conclusions are as follows:

(1) The field is concentrated at micro and meso voxels (48 and 50 of 140 records); amount/size metrics account for 222 of the 489 study–metric pairs; the physically decisive sub-micron class holds only eleven studies; and formal shape descriptors and spatial statistics are rarely measured, although these are precisely the families that mechanistic arguments and performance-linked studies implicate in strength and transport behavior.

(2) The seven cross-scale discrepancies—resolution-conditioned porosity, the REV–resolution dilemma, segmentation variance comparable to material effects, resolution-biased and under-used shape metrics, the near-absence of spatial statistics, terminology drift, and the new void classes and metrics created by new processes—reduce to three conditioning elements (the observation window, the resolved population and the descriptor definition) so the principal obstacles to cumulative knowledge are methodological rather than instrumental. Voxel-size-conditioned metrics are the largest and least correctable distortion; unreported segmentation sensitivity is repayable at publication time; the under-use of shape and spatial descriptors is removable by adoption alone; volumes below the REV of the reported quantity call for registered multiscale acquisition.

(3) Comparability requires the metric-conditional minimum-reporting checklist of Table 5, applied as a floor rather than a target, together with the seven research priorities identified here. None of these obstacles requires instruments based on new physical principles, although sub-micron, phase-contrast and in situ CT and registered multi-resolution acquisition may require facilities beyond a standard laboratory; the sub-micron coverage gap is therefore a question of access to existing nano-CT and synchrotron facilities rather than of instrument development. The classified corpus provides the map, synthesized in Figure 19, and the priorities chart the route toward CT pore analysis as a quantitative, reproducible and scale-aware discipline.

Author Contributions: Conceptualization, M.K., M.H. and H.S.; methodology, H.S.; data curation, M.K. and M.H.; formal analysis, M.K. and M.H.; visualization, M.K. and M.H.; writing—original draft preparation, M.K. and M.H.; writing—review and editing, S.-C.B. and H.S.; supervision, H.S.; funding acquisition, H.S. All authors have read and agreed to the published version of the manuscript.

Funding: This work was supported by the National Research Foundation of Korea (NRF) grant funded by the Korea government (MSIT) through the Sejong Science Fellowship (No. RS-2025-00560972). This research was also supported by a grant from the Land, Infrastructure and Transport Technology R&D Program for Early Career Researchers funded by the Ministry of Land, Infrastructure and Transport (MOLIT)/Korea Agency for Infrastructure Technology Advancement (KAIA) (Grant No. RS-2026-25528175).

Data Availability Statement: The data presented in this study—the complete classified corpus (bibliographic metadata, voxel-size class, material domain and metric coding for all 206 references, with stable identifiers R001–R206) together with a codebook documenting column definitions, the mapping between dataset labels and manuscript terminology, the application/methodology split rule and the moving-average specification of Figure 13—are available on request from the corresponding author.

Conflicts of Interest: The authors declare no conflicts of interest. The funders had no role in the design of the study; in the collection, analyses, or interpretation of data; in the writing of the manuscript; or in the decision to publish the results.

Abbreviations

The following abbreviations are used in this manuscript:

4D CT	time-resolved computed tomography (3D + time)
ASTM	American Society for Testing and Materials (standards body)
BSE	backscattered electron (imaging)
CNN	convolutional neural network
CT	computed tomography
D10/D50/D90	10th/50th/90th-percentile diameters of the cumulative pore-size distribution
DVC	digital volume correlation
FOV	field of view
ITZ	interfacial transition zone
LBM	lattice Boltzmann method
LSCM	laser scanning confocal microscopy
MIL	mean intercept length
MIP	mercury intrusion porosimetry
OPC	ordinary Portland cement
PSD	pore-size distribution
RAC	recycled-aggregate concrete
RDF	radial distribution function
REV	representative elementary volume
SEM	scanning electron microscopy
UHPC	ultra-high-performance concrete
VOI	volume of interest

References

1. Suh, H.; Cho, S.; Her, S.; Bae, S. Influence of multi-scale three-dimensional pore characteristics on the mechanical properties of graphene oxide and carbon nanotube incorporated cement paste. *Cem. Concr. Res.* **2023**, *174*, 107326. [CrossRef]
2. Chen, Y.; Tang, C.; Cui, M.; Sun, L.; Liu, M.; Sun, G. Predicting compressive strength of foamed concrete based on anisotropy of the pore structure with the influence of pore size and shape using X-ray computed tomography. *ACS Omega* **2026**, *11*, 21232–21245. [CrossRef] [PubMed]
3. van den Heever, M.; du Plessis, A.; Kruger, J.; van Zijl, G. Evaluating the effects of porosity on the mechanical properties of extrusion-based 3D printed concrete. *Cem. Concr. Res.* **2022**, *153*, 106695. [CrossRef]
4. Luo, Q.; Liu, D.; Qiao, P.; Zhou, Z.; Zhao, Y.; Sun, L. Micro-CT-based micromechanics and numerical homogenization for effective elastic property of ultra-high performance concrete. *Int. J. Damage Mech.* **2019**, *29*, 45–66. [CrossRef]
5. Shan, J.; Zhang, Y.; Wu, S.; Lin, Z.; Li, L.; Wu, Q. Pore characteristics of pervious concrete and their influence on permeability attributes. *Constr. Build. Mater.* **2022**, *327*, 126874. [CrossRef]
6. Yuan, J.; Chen, W.; Tan, X.; Yang, W.; Yang, D.; Yu, H.; Zhou, B.; Yang, B. Study on the permeability characteristics of foamed concrete using a pore-scale model from X-ray microcomputed tomography image reconstruction and numerical simulation. *J. Mater. Civ. Eng.* **2021**, *33*, 04021117. [CrossRef]
7. Vigor, J.E.; Prentice, D.P.; Xiao, X.; Bernal, S.A.; Provis, J.L. The pore structure and water absorption in Portland/slag blended hardened cement paste determined by synchrotron X-ray microtomography and neutron radiography. *RSC Adv.* **2024**, *14*, 4389–4405. [CrossRef] [PubMed]
8. Zhang, Y.; Zhang, Y.; Yang, L.; Liu, G.; Du, H. Influence of the pore feature on the water uptake in 3D printed concrete. *Mater. Lett.* **2023**, *333*, 133642. [CrossRef]
9. Tian, Z.; Zhu, X.; Chen, X.; Ning, Y.; Zhang, W. Microstructure and damage evolution of hydraulic concrete exposed to freeze–thaw cycles. *Constr. Build. Mater.* **2022**, *346*, 128466. [CrossRef]
10. Krstic, M.; Davalos, J.F.; Rossi, E.; Figueiredo, S.C.; Copuroglu, O. Freeze–thaw resistance and air-void analysis of concrete with recycled glass–pozzolan using X-ray micro-tomography. *Materials* **2020**, *14*, 154. [CrossRef] [PubMed]
11. Tian, Y.; Jiang, H.; Fan, X.; Zhang, G.; Jin, N.; Zeng, Q.; Jin, X.; Yan, D.; Peng, Y.; Wang, J. Corrosion damages of reinforced concrete characterized by X-ray CT and DVC techniques. *Constr. Build. Mater.* **2023**, *409*, 134218. [CrossRef]
12. Taheri-Shakib, J.; Al-Mayah, A. Applications of X-ray computed tomography to characterize corrosion-induced cracking evolution in reinforced concrete: A review. *J. Build. Eng.* **2024**, *90*, 109420. [CrossRef]

13. Kim, J.-S.; Youm, K.S.; Lim, J.-H.; Han, T.-S. Effect of carbonation on cement paste microstructure characterized by micro-computed tomography. *Constr. Build. Mater.* **2020**, *263*, 120079. [CrossRef]
14. Zhang, H.; Romero Rodriguez, C.; Dong, H.; Gan, Y.; Schlangen, E.; Šavija, B. Elucidating the effect of accelerated carbonation on porosity and mechanical properties of hydrated Portland cement paste using X-ray tomography and advanced micromechanical testing. *Micromachines* **2020**, *11*, 471. [CrossRef] [PubMed]
15. Shakoorioskooie, M.; Griffa, M.; Leemann, A.; Zboray, R.; Lura, P. Alkali-silica reaction products and cracks: X-ray micro-tomography-based analysis of their spatial-temporal evolution at a mesoscale. *Cem. Concr. Res.* **2021**, *150*, 106593. [CrossRef]
16. Stock, S.R.; Naik, N.K.; Wilkinson, A.P.; Kurtis, K.E. X-ray microtomography (microCT) of the progression of sulfate attack of cement paste. *Cem. Concr. Res.* **2002**, *32*, 1673–1675, Correction in *Cem. Concr. Res.* **2002**, *32*, 1997. [CrossRef]
17. Chen, Y.; Çopuroğlu, O.; Romero Rodriguez, C.; Mendonca Filho, F.F.; Schlangen, E. Characterization of air-void systems in 3D printed cementitious materials using optical image scanning and X-ray computed tomography. *Mater. Charact.* **2021**, *173*, 110948. [CrossRef]
18. Luo, R.; Sun, B.; Fei, X.; Du, H. Interlayer strength loss in 3D printed concrete due to time-gap-induced macroporosity. *Constr. Build. Mater.* **2025**, *497*, 143924. [CrossRef]
19. Brisard, S.; Serdar, M.; Monteiro, P.J.M. Multiscale X-ray tomography of cementitious materials: A review. *Cem. Concr. Res.* **2020**, *128*, 105824. [CrossRef]
20. Chung, S.-Y.; Kim, J.-S.; Stephan, D.; Han, T.-S. Overview of the use of micro-computed tomography (micro-CT) to investigate the relation between the material characteristics and properties of cement-based materials. *Constr. Build. Mater.* **2019**, *229*, 116843. [CrossRef]
21. Luo, Z.; Jiao, L. Experimental, computational, and simulation methods for investigating the pore connectivity of cement-based materials: A review. *Front. Mater.* **2025**, *12*, 1664496. [CrossRef]
22. Song, Y.; Zhou, J.-W.; Bian, Z.-N.; Dai, G.-Z. Pore structure characterization of hardened cement paste by multiple methods. *Adv. Mater. Sci. Eng.* **2019**, *2019*, 3726953. [CrossRef]
23. Wang, X.; Peng, Y.; Wang, J.; Zeng, Q. Pore structure damages in cement-based materials by mercury intrusion: A non-destructive assessment by X-ray computed tomography. *Materials* **2019**, *12*, 2220. [CrossRef] [PubMed]
24. Xue, S.; Zhang, P.; Bao, J.; He, L.; Hu, Y.; Yang, S. Comparison of mercury intrusion porosimetry and multi-scale X-ray CT on characterizing the microstructure of heat-treated cement mortar. *Mater. Charact.* **2020**, *160*, 110085. [CrossRef]
25. Zhu, J.; Zhang, R.; Zhang, Y.; He, F. The fractal characteristics of pore size distribution in cement-based materials and its effect on gas permeability. *Sci. Rep.* **2019**, *9*, 17191. [CrossRef] [PubMed]
26. Gallucci, E.; Scrivener, K.; Groso, A.; Stampanoni, M.; Margaritondo, G. 3D experimental investigation of the microstructure of cement pastes using synchrotron X-ray microtomography (μCT). *Cem. Concr. Res.* **2007**, *37*, 360–368. [CrossRef]
27. Cnudde, V.; Boone, M.N. High-resolution X-ray computed tomography in geosciences: A review of the current technology and applications. *Earth-Sci. Rev.* **2013**, *123*, 1–17. [CrossRef]
28. Maire, E.; Withers, P.J. Quantitative X-ray tomography. *Int. Mater. Rev.* **2014**, *59*, 1–43. [CrossRef]
29. Withers, P.J.; Bouman, C.; Carmignato, S.; Cnudde, V.; Grimaldi, D.; Hagen, C.K.; Maire, E.; Manley, M.; du Plessis, A.; Stock, S.R. X-ray computed tomography. *Nat. Rev. Methods Primers* **2021**, *1*, 18. [CrossRef]
30. Promentilla, M.A.B.; Sugiyama, T.; Hitomi, T.; Takeda, N. Quantification of tortuosity in hardened cement pastes using synchrotron-based X-ray computed microtomography. *Cem. Concr. Res.* **2009**, *39*, 548–557. [CrossRef]
31. Sugiyama, T.; Promentilla, M.A.B.; Hitomi, T.; Takeda, N. Application of synchrotron microtomography for pore structure characterization of deteriorated cementitious materials due to leaching. *Cem. Concr. Res.* **2010**, *40*, 1265–1270. [CrossRef]
32. Abera, K.A.; Manahiloh, K.N.; Motalleb Nejad, M. The effectiveness of global thresholding techniques in segmenting two-phase porous media. *Constr. Build. Mater.* **2017**, *142*, 256–267. [CrossRef]
33. Deboodt, T.; Wildenschild, D.; Ideker, J.H.; Burkan Isgor, O. Comparison of thresholding techniques for quantifying Portland cement hydrates using synchrotron microtomography. *Constr. Build. Mater.* **2021**, *266*, 121109. [CrossRef]
34. Iassonov, P.; Gebrenegus, T.; Tuller, M. Segmentation of X-ray computed tomography images of porous materials: A crucial step for characterization and quantitative analysis of pore structures. *Water Resour. Res.* **2009**, *45*, W09415. [CrossRef]
35. Liu, C.; Chen, Z.; Lv, Q.; Liang, M.; Zhang, Y. Multiscale pore structure segmentation of cementitious materials using light-weight and modified VGG-Unet network. *J. Build. Eng.* **2025**, *111*, 113618. [CrossRef]
36. Dong, H.; Blunt, M.J. Pore-network extraction from micro-computerized-tomography images. *Phys. Rev. E* **2009**, *80*, 036307. [CrossRef] [PubMed]
37. Gostick, J.T. Versatile and efficient pore network extraction method using marker-based watershed segmentation. *Phys. Rev. E* **2017**, *96*, 023307. [CrossRef] [PubMed]
38. Otsu, N. A threshold selection method from gray-level histograms. *IEEE Trans. Syst. Man Cybern.* **1979**, *9*, 62–66. [CrossRef]
39. Silin, D.; Patzek, T. Pore space morphology analysis using maximal inscribed spheres. *Phys. A* **2006**, *371*, 336–360. [CrossRef]

40. Chica, L.; Mera, C.; Sepúlveda-Cano, L.M.; Alzate, A. Porosity estimation and pore structure characterization of foamed cement paste using non-specialized image digital processing. *Mater. Struct.* **2022**, *55*, 189. [CrossRef]
41. Qian, H.; Li, Y.; Yang, J.; Xie, L.; Tan, K.H. Segmentation and analysis of cement particles in cement paste with deep learning. *Cem. Concr. Compos.* **2023**, *136*, 104819. [CrossRef]
42. Liu, J.; Ma, K.; Shen, J.; Zhu, J.; Long, G.; Xie, Y.; Liu, B. Influence of recycled concrete aggregate enhancement methods on the change of microstructure of ITZs in recycled aggregate concrete. *Constr. Build. Mater.* **2023**, *371*, 130772. [CrossRef]
43. Lu, C.; Yu, Q.; Wei, J.; Niu, Y.; Zhang, Y.; Lin, C.; Chen, P.; Shi, C.; Yang, P. Influence of interface transition zones (ITZ) and pore structure on the compressive strength of recycled aggregate concrete. *Constr. Build. Mater.* **2024**, *456*, 139299. [CrossRef]
44. Wang, P.; Chen, B.; Hashmi, A.; Yao, X.; Dong, J. Two-stage deterioration mechanisms in recycled aggregate concrete: From pore interface degradation to aggregate interface defect control. *Buildings* **2025**, *15*, 4480. [CrossRef]
45. Zhang, S.; Tan, G.; Qi, Z.; Tian, B.; Cao, J.; Chen, B. Relationship between the carbonation depth and microstructure of concrete under freeze–thaw conditions. *Materials* **2024**, *17*, 6191. [CrossRef] [PubMed]
46. Li, Y.; Shen, A.; Wu, H. Fractal dimension of basalt fiber reinforced concrete (BFRC) and its correlations to pore structure, strength and shrinkage. *Materials* **2020**, *13*, 3238. [CrossRef] [PubMed]
47. Bai, M.; Xiao, J.; Gao, Y.; Ding, T. Pore structure characteristics and mechanical property of engineered cementitious composites (ECC) incorporating recycled sand. *Constr. Build. Mater.* **2023**, *408*, 133721. [CrossRef]
48. Jiang, Y.; Lawrence, M.; Ansell, M.P.; Hussain, A. Cell wall microstructure, pore size distribution and absolute density of hemp shiv. *R. Soc. Open Sci.* **2018**, *5*, 171945. [CrossRef] [PubMed]
49. Adrien, J.; Meille, S.; Tadier, S.; Maire, E.; Sasaki, L. In-situ X-ray tomographic monitoring of gypsum plaster setting. *Cem. Concr. Res.* **2016**, *82*, 107–116. [CrossRef]
50. Bennai, F.; El Hachem, C.; Abahri, K.; Belarbi, R. Microscopic hydric characterization of hemp concrete by X-ray microtomography and digital volume correlation. *Constr. Build. Mater.* **2018**, *188*, 983–994. [CrossRef]
51. Brunello, V.; Canevali, C.; Corti, C.; de Kock, T.; Rampazzi, L.; Recchia, S.; Sansonetti, A.; Tedeschi, C.; Cnudde, V. Understanding the microstructure of mortars for cultural heritage using X-ray CT and MIP. *Materials* **2021**, *14*, 5939. [CrossRef] [PubMed]
52. Liu, J.; Khieu, H.H.; Van Tran, M.; Tran, P. Advancing microstructural insights in 3D-printed cementitious materials via X-ray micro-computed tomography. *J. Build. Eng.* **2025**, *107*, 112675. [CrossRef]
53. Bossa, N.; Chaurand, P.; Vicente, J.; Borschneck, D.; Levard, C.; Aguerre-Chariol, O.; Rose, J. Micro- and nano-X-ray computed-tomography: A step forward in the characterization of the pore network of a leached cement paste. *Cem. Concr. Res.* **2015**, *67*, 138–147. [CrossRef]
54. Su, Z.; Yue, Z.; Stamati, O.; Villanova, J.; Burnett, T.L.; Provis, J.L.; Paul, P.P.; Bernal, S.A.; Withers, P.J. Quantifying resolution-dependent microstructure and pore-network topology in LDH-modified alkali-activated slag pastes via synchrotron X-ray nano-holotomography and multiscale tomography. *Cem. Concr. Res.* **2026**, *203*, 108173. [CrossRef]
55. Wu, Z.; Wei, Y.; Wang, S.; Chen, J. Application of X-ray micro-CT for quantifying degree of hydration of slag-blended cement paste. *J. Mater. Civ. Eng.* **2020**, *32*, 04020008. [CrossRef]
56. Kim, J.-S.; Suh, J.; Pae, J.; Moon, J.; Han, T.-S. Gradient-based phase segmentation method for characterization of hydrating cement paste microstructures obtained from X-ray micro-CT. *J. Build. Eng.* **2022**, *46*, 103721. [CrossRef]
57. Chen, Y.; Ning, Y.; Chen, X.; Xuan, W.; Guo, Y. Experimental investigation on the effect of curing condition and admixture on meso-structure of recycled aggregate concrete based on X-ray CT. *Int. J. Concr. Struct. Mater.* **2023**, *17*, 11. [CrossRef]
58. Olawuyi, B.J.; Boshoff, W.P. Influence of SAP content and curing age on air void distribution of high performance concrete using 3D volume analysis. *Constr. Build. Mater.* **2017**, *135*, 580–589. [CrossRef]
59. Chandrappa, A.K.; Biligiri, K.P. Pore structure characterization of pervious concrete using X-ray microcomputed tomography. *J. Mater. Civ. Eng.* **2018**, *30*, 04018108. [CrossRef]
60. Yavuz, D.; Yazıcı, Ş.; Avcı, M.S.; Özmen, D. A novel approach to estimate the tortuosity of pervious concretes using computed tomography. *Mater. Struct.* **2023**, *56*, 74. [CrossRef]
61. Li, H.; Yang, J.; Yu, X.; Zhang, Y.; Zhang, L. Permeability prediction of pervious concrete based on mix proportions and pore characteristics. *Constr. Build. Mater.* **2023**, *395*, 132247. [CrossRef]
62. Parisatto, M.; Dalconi, M.C.; Valentini, L.; Artioli, G.; Rack, A.; Tucoulou, R.; Cruciani, G.; Ferrari, G. Examining microstructural evolution of Portland cements by in-situ synchrotron micro-tomography. *J. Mater. Sci.* **2014**, *50*, 1805–1817. [CrossRef]
63. Zhuang, L.; Shin, H.-S.; Yeom, S.; Pham, C.N.; Kim, Y.-J. A novel method for estimating subresolution porosity from CT images and its application to homogeneity evaluation of porous media. *Sci. Rep.* **2022**, *12*, 16229. [CrossRef] [PubMed]
64. Matsuno, A.; Ishizuka, S.; Nguyen, T.L.; Dung, N.T.; Nguyen, V.T.; Nguyen, H.G.; Kawamoto, K. Comparison of macropore structures and networks of autoclaved aerated concrete blocks using micro-focus X-ray computed tomography. *Int. J. GEOMATE* **2020**, *19*, 160–165. [CrossRef]
65. Salcedo, I.R.; Cuesta, A.; Shirani, S.; León-Reina, L.; Aranda, M.A.G. Accuracy in cement hydration investigations: Combined X-ray microtomography and powder diffraction analyses. *Materials* **2021**, *14*, 6953. [CrossRef] [PubMed]

66. Stelzner, L.; Powierza, B.; Oesch, T.; Dlugosch, R.; Weise, F. Thermally-induced moisture transport in high-performance concrete studied by X-ray-CT and 1H-NMR. *Constr. Build. Mater.* **2019**, *224*, 600–609. [CrossRef]
67. Hong, S.; Liu, P.; Zhang, J.; Xing, F.; Dong, B. Visual & quantitative identification of cracking in mortar subjected to loads using X-ray computed tomography method. *Cem. Concr. Compos.* **2019**, *100*, 15–24. [CrossRef]
68. Li, N.; Zhao, Y.; Xing, Y.; He, X.; Li, H. Meso-damage analysis of concrete based on X-ray CT in-situ compression and using deep learning method. *Case Stud. Constr. Mater.* **2023**, *18*, e02118. [CrossRef]
69. Lorenzoni, R.; Curosu, I.; Léonard, F.; Paciornik, S.; Mechtcherine, V.; Silva, F.A.; Bruno, G. Combined mechanical and 3D-microstructural analysis of strain-hardening cement-based composites (SHCC) by in-situ X-ray microtomography. *Cem. Concr. Res.* **2020**, *136*, 106139. [CrossRef]
70. Zhao, Y.; Li, N.; Niu, H.; Shi, J. Study on in-situ CT damage of concrete subjected to compressive loading after freeze-thaw cycles based on deep learning and DVC technology. *Constr. Build. Mater.* **2025**, *482*, 141599. [CrossRef]
71. Chen, J.; He, Z.; Chen, S.; Nguyen, P.M.V.; Liu, J.; Xu, H. Study on freeze-thaw damage of surface and pore structure of steam cured concrete. *Sci. Rep.* **2025**, *15*, 22594. [CrossRef] [PubMed]
72. Sokhansefat, G.; Moradian, M.; Finnell, M.; Behravan, A.; Ley, M.T.; Lucero, C.; Weiss, J. Using X-ray computed tomography to investigate mortar subjected to freeze-thaw cycles. *Cem. Concr. Compos.* **2020**, *108*, 103520. [CrossRef]
73. Fan, S.; Li, M. X-ray computed microtomography of three-dimensional microcracks and self-healing in engineered cementitious composites. *Smart Mater. Struct.* **2014**, *24*, 015021. [CrossRef]
74. Fang, G.; Liu, Y.; Qin, S.; Ding, W.; Zhang, J.; Hong, S.; Xing, F.; Dong, B. Visualized tracing of crack self-healing features in cement/microcapsule system with X-ray microcomputed tomography. *Constr. Build. Mater.* **2018**, *179*, 336–347. [CrossRef]
75. He, J.; Deng, Y.; Shi, X. Quantitative analysis of pore structures and microcracks in self-healing concrete after freeze-thaw exposure: An X-ray computed tomography-based approach. *Cem. Concr. Compos.* **2025**, *162*, 106105. [CrossRef]
76. Suleiman, A.R.; Nehdi, M.L. Effect of autogenous crack self-healing on mechanical strength recovery of cement mortar under various environmental exposure. *Sci. Rep.* **2021**, *11*, 7245. [CrossRef] [PubMed]
77. Wang, J.; Dewanckele, J.; Cnudde, V.; Van Vlierberghe, S.; Verstraete, W.; De Belie, N. X-ray computed tomography proof of bacterial-based self-healing in concrete. *Cem. Concr. Compos.* **2014**, *53*, 289–304. [CrossRef]
78. Yio, M.H.N.; Wong, H.S.; Buenfeld, N.R. Representative elementary volume (REV) of cementitious materials from three-dimensional pore structure analysis. *Cem. Concr. Res.* **2017**, *102*, 187–202. [CrossRef]
79. Fan, M.; Chen, Y.; Wan, K. Representative elementary volume analysis of hardened cement paste during hydration using X-ray computed tomography. *Constr. Build. Mater.* **2021**, *277*, 122268. [CrossRef]
80. Wildenschild, D.; Sheppard, A.P. X-ray imaging and analysis techniques for quantifying pore-scale structure and processes in subsurface porous medium systems. *Adv. Water Resour.* **2013**, *51*, 217–246. [CrossRef]
81. Kim, K.Y.; Yun, T.S.; Choo, J.; Kang, D.H.; Shin, H.S. Determination of air-void parameters of hardened cement-based materials using X-ray computed tomography. *Constr. Build. Mater.* **2012**, *37*, 93–101. [CrossRef]
82. Houston, A.N.; Otten, W.; Baveye, P.C.; Hapca, S. Adaptive-window indicator kriging: A thresholding method for computed tomography images of porous media. *Comput. Geosci.* **2013**, *54*, 239–248. [CrossRef]
83. Oh, W.; Lindquist, B. Image thresholding by indicator kriging. *IEEE Trans. Pattern Anal. Mach. Intell.* **1999**, *21*, 590–602. [CrossRef]
84. Kornilov, A.; Safonov, I.; Yakimchuk, I. A review of watershed implementations for segmentation of volumetric images. *J. Imaging* **2022**, *8*, 127. [CrossRef] [PubMed]
85. Chung, S.-Y.; Sikora, P.; Rucinska, T.; Stephan, D.; Abd Elrahman, M. Comparison of the pore size distributions of concretes with different air-entraining admixture dosages using 2D and 3D imaging approaches. *Mater. Charact.* **2020**, *162*, 110182. [CrossRef]
86. Chauhan, S.; Rühaak, W.; Khan, F.; Enzmann, F.; Mielke, P.; Kersten, M.; Sass, I. Processing of rock core microtomography images: Using seven different machine learning algorithms. *Comput. Geosci.* **2016**, *86*, 120–128. [CrossRef]
87. Karimpouli, S.; Tahmasebi, P. Segmentation of digital rock images using deep convolutional autoencoder networks. *Comput. Geosci.* **2019**, *126*, 142–150. [CrossRef]
88. Karimpouli, S.; Tahmasebi, P.; Saenger, E.H. Coal cleat/fracture segmentation using convolutional neural networks. *Nat. Resour. Res.* **2019**, *29*, 1675–1685. [CrossRef]
89. Zhang, P.; Lu, S.; Li, J.; Zhang, P.; Xie, L.; Xue, H.; Zhang, J. Multi-component segmentation of X-ray computed tomography (CT) image using multi-Otsu thresholding algorithm and scanning electron microscopy. *Energy Explor. Exploit.* **2017**, *35*, 281–294. [CrossRef]
90. Lorenzoni, R.; Curosu, I.; Paciornik, S.; Mechtcherine, V.; Oppermann, M.; Silva, F. Semantic segmentation of the micro-structure of strain-hardening cement-based composites (SHCC) by applying deep learning on micro-computed tomography scans. *Cem. Concr. Compos.* **2020**, *108*, 103551. [CrossRef]
91. Liu, H.; Zhu, E.; Ji, M.; Bai, Z.; Li, T. Quantification of total porosity from CT images by segmenting unhydrated cement: A model-informed framework integrating Powers' volume model. *Materials* **2026**, *19*, 686. [CrossRef] [PubMed]

92. Qian, L.-P.; Li, X.-Y.; Bai, Y.-L.; Guo, K.; Wang, J.; Chen, D.; Li, Y.; Li, Y.; Du, X. Deep learning-driven microstructural image analysis: Recent advances in cementitious materials. *J. Build. Eng.* **2026**, *123*, 115845. [CrossRef]
93. Rezaei, F.; Izadi, H.; Memarian, H.; Baniassadi, M. The effectiveness of different thresholding techniques in segmenting micro CT images of porous carbonates to estimate porosity. *J. Pet. Sci. Eng.* **2019**, *177*, 518–527. [CrossRef]
94. Tretiak, I.; Smith, R.A. A parametric study of segmentation thresholds for X-ray CT porosity characterisation in composite materials. *Compos. Part A Appl. Sci. Manuf.* **2019**, *123*, 10–24. [CrossRef]
95. Promentilla, M.A.B.; Cortez, S.M.; Papel, R.A.D.; Tablada, B.M.; Sugiyama, T. Evaluation of microstructure and transport properties of deteriorated cementitious materials from their X-ray computed tomography (CT) images. *Materials* **2016**, *9*, 388. [CrossRef] [PubMed]
96. Gerke, K.M.; Sizonenko, T.O.; Karsanina, M.V.; Lavrukhin, E.V.; Abashkin, V.V.; Korost, D.V. Improving watershed-based pore-network extraction method using maximum inscribed ball pore-body positioning. *Adv. Water Resour.* **2020**, *140*, 103576. [CrossRef]
97. Hayatdavoudi, M.; Niri, M.E.; Kalhor, A. Comparative analysis of sandstone microtomographic image segmentation using advanced convolutional neural networks with pixelwise and physical accuracy evaluation. *Sci. Rep.* **2025**, *15*, 22164. [CrossRef] [PubMed]
98. Wang, Y.; Blunt, M.J.; Armstrong, R.T.; Mostaghimi, P. Deep learning in pore scale imaging and modeling. *Earth-Sci. Rev.* **2021**, *215*, 103555. [CrossRef]
99. Costanza-Robinson, M.S.; Estabrook, B.D.; Fouhey, D.F. Representative elementary volume estimation for porosity, moisture saturation, and air-water interfacial areas in unsaturated porous media: Data quality implications. *Water Resour. Res.* **2011**, *47*, W07513. [CrossRef]
100. Singh, A.; Regenauer-Lieb, K.; Walsh, S.D.C.; Armstrong, R.T.; van Griethuysen, J.J.M.; Mostaghimi, P. On representative elementary volumes of grayscale micro-CT images of porous media. *Geophys. Res. Lett.* **2020**, *47*, e2020GL088594. [CrossRef]
101. Cooper, D.; Turinsky, A.; Sensen, C.; Hallgrimsson, B. Effect of voxel size on 3D micro-CT analysis of cortical bone porosity. *Calcif. Tissue Int.* **2007**, *80*, 211–219. [CrossRef] [PubMed]
102. Paganin, D.; Mayo, S.C.; Gureyev, T.E.; Miller, P.R.; Wilkins, S.W. Simultaneous phase and amplitude extraction from a single defocused image of a homogeneous object. *J. Microsc.* **2002**, *206*, 33–40. [CrossRef] [PubMed]
103. Fan, S.; Ren, H.; Hong, S.; Xing, F.; Hou, D.; Dong, B. Interfacial mechanical bond characterization between cement pastes and porous aggregates through a coupled XCT and DVC technique. *Cem. Concr. Compos.* **2023**, *142*, 105158. [CrossRef]
104. Li, N.; Zhao, Y.; Xing, Y.; He, X. Localized damage analysis of cement mortar using X-ray computed tomography in situ compressive loading and digital volume correlation. *Appl. Sci.* **2023**, *13*, 3842. [CrossRef]
105. Doube, M.; Kłosowski, M.M.; Arganda-Carreras, I.; Cordelières, F.P.; Dougherty, R.P.; Jackson, J.S.; Schmid, B.; Hutchinson, J.R.; Shefelbine, S.J. BoneJ: Free and extensible bone image analysis in ImageJ. *Bone* **2010**, *47*, 1076–1079. [CrossRef] [PubMed]
106. Gostick, J.T.; Khan, Z.A.; Tranter, T.G.; Kok, M.D.R.; Agnaou, M.; Sadeghi, M.; Jervis, R. PoreSpy: A Python toolkit for quantitative analysis of porous media images. *J. Open Source Softw.* **2019**, *4*, 1296. [CrossRef]
107. Al-Raoush, R.I.; Madhoun, I.T. TORT3D: A MATLAB code to compute geometric tortuosity from 3D images of unconsolidated porous media. *Powder Technol.* **2017**, *320*, 99–107. [CrossRef]
108. Koenig, A. Analysis of air voids in cementitious materials using micro X-ray computed tomography (μXCT). *Constr. Build. Mater.* **2020**, *244*, 118313. [CrossRef]
109. Wang, Y.; Xie, S.; Li, Y.; Yang, M.; Chen, Q.; Huang, L.; Hu, D.; Li, S. Advanced pore structure characterization of high-volume mineral admixture steam-cured mortar using X-ray computed tomography. *Materials* **2025**, *18*, 1575. [CrossRef] [PubMed]
110. Chen, Y.; Kuva, J.; Mohite, A.; Li, Z.; Rahier, H.; Al-Neshawy, F.; Shu, J. Investigation of the internal structure of hardened 3D-printed concrete by X-CT scanning and its influence on the mechanical performance. *Materials* **2023**, *16*, 2534. [CrossRef] [PubMed]
111. Mohan, M.K.; Rahul, A.V.; Van Stappen, J.F.; Cnudde, V.; De Schutter, G.; Van Tittelboom, K. Assessment of pore structure characteristics and tortuosity of 3D printed concrete using mercury intrusion porosimetry and X-ray tomography. *Cem. Concr. Compos.* **2023**, *140*, 105104. [CrossRef]
112. Zhao, D.; Xu, J.; Han, Z.; Liu, Y.; Liu, Y.; Yang, X. Study on the correlation between pore structure characterization and early mechanical properties of foamed concrete based on X-CT. *Constr. Build. Mater.* **2024**, *450*, 138603. [CrossRef]
113. Fu, J.; Yu, Y. Experimental study on pore characteristics and fractal dimension calculation of pore structure of aerated concrete block. *Adv. Civ. Eng.* **2019**, *2019*, 8043248. [CrossRef]
114. Xin, C.; Yang, Y.; Yang, M.; Di, J.; Sun, Y.; Liang, P.; Wang, Y. Multi-scale analysis of the damage evolution of coal gangue coarse aggregate concrete after freeze–thaw cycle based on CT technology. *Materials* **2024**, *17*, 975. [CrossRef] [PubMed]
115. Li, F.; Luo, D.; Niu, D. Durability evaluation of concrete structure under freeze-thaw environment based on pore evolution derived from deep learning. *Constr. Build. Mater.* **2025**, *467*, 140422. [CrossRef]

116. Ma, H.; Fu, C.; Wu, J.; Yuan, X.; Wu, C.; Feng, J. Micro/meso scales characterization of alkali-activated fly ash-slag concrete under sustained high-temperatures with X-CT, MIP, and SEM tests. *Mater. Today Sustain.* **2024**, *28*, 101036. [CrossRef]
117. Yuan, J.; Wu, Y.; Zhang, J. Characterization of air voids and frost resistance of concrete based on industrial computerized tomographical technology. *Constr. Build. Mater.* **2018**, *168*, 975–983. [CrossRef]
118. Yun, T.S.; Kim, K.Y.; Choo, J.; Kang, D.H. Quantifying the distribution of paste-void spacing of hardened cement paste using X-ray computed tomography. *Mater. Charact.* **2012**, *73*, 137–143. [CrossRef]
119. Lyu, K.; Garboczi, E.J.; Liu, X. A quantitative characterization of spatial arrangement of air voids in mortars via X-ray CT and numerical calculations. *Constr. Build. Mater.* **2022**, *360*, 129550. [CrossRef]
120. Chen, Y.; Zhang, Y.; Xie, Y.; Zhang, Z.; Banthia, N. Unraveling pore structure alternations in 3D-printed geopolymer concrete and corresponding impacts on macro-properties. *Addit. Manuf.* **2022**, *59*, 103137. [CrossRef]
121. Moini, M.; Olek, J.; Youngblood, J.P.; Magee, B.; Zavattieri, P.D. Additive manufacturing and performance of architectured cement-based materials. *Adv. Mater.* **2018**, *30*, 1802123. [CrossRef] [PubMed]
122. Zhang, X.; Yang, Z.; Pang, M.; Yao, Y.; Li, Q.M.; Marrow, T.J. Ex-situ micro X-ray computed tomography tests and image-based simulation of UHPFRC beams under bending. *Cem. Concr. Compos.* **2021**, *123*, 104216. [CrossRef]
123. Liu, H.; Tao, Y.; Zhu, C.; Liu, C.; Wang, Y.; Yun, J.; Zhang, Y. 3D printed concrete with recycled coarse aggregate: Freeze–thaw resistance assessment and damage mechanisms. *Cem. Concr. Res.* **2026**, *200*, 108095. [CrossRef]
124. Ngo, T.H.; Li, S.; Huynh, T.; Zhang, Y.X.; Tran, P. 3D printable hemp concrete: Rheological, mechanical, and microstructural properties. *J. Build. Eng.* **2025**, *114*, 114467. [CrossRef]
125. Clennell, M.B. Tortuosity: A guide through the maze. *Geol. Soc. Lond. Spec. Publ.* **1997**, *122*, 299–344. [CrossRef]
126. Epstein, N. On tortuosity and the tortuosity factor in flow and diffusion through porous media. *Chem. Eng. Sci.* **1989**, *44*, 777–779. [CrossRef]
127. Ghanbarian, B.; Hunt, A.G.; Ewing, R.P.; Sahimi, M. Tortuosity in porous media: A critical review. *Soil Sci. Soc. Am. J.* **2013**, *77*, 1461–1477. [CrossRef]
128. Zhao, Z.; Zhou, X.-P. Digital analysis for pore-scale compressive strength and permeability of foamed cement with realistic microstructures by X-ray-μCT imaging. *Constr. Build. Mater.* **2022**, *346*, 128456. [CrossRef]
129. Osipov, S.; Prischepa, I. Algorithm of estimation of the degree of porosity homogeneity of foamed concretes by local volumes by X-ray computed tomography method. *Materials* **2023**, *16*, 3244. [CrossRef] [PubMed]
130. Yoon, J.; Kim, H.; Sim, S.-H.; Pyo, S. Characterization of porous cementitious materials using microscopic image processing and X-ray CT analysis. *Materials* **2020**, *13*, 3105. [CrossRef] [PubMed]
131. Petlitckaia, S.; Vincente, J.; Poulesquen, A. Characterization of a geopolymer foam by X-ray tomography. *Front. Chem.* **2021**, *9*, 754355. [CrossRef] [PubMed]
132. Blott, S.J.; Pye, K. Particle shape: A review and new methods of characterization and classification. *Sedimentology* **2007**, *55*, 31–63. [CrossRef]
133. Schmitt, M.; Halisch, M.; Müller, C.; Fernandes, C.P. Classification and quantification of pore shapes in sandstone reservoir rocks with 3-D X-ray micro-computed tomography. *Solid Earth* **2016**, *7*, 285–300. [CrossRef]
134. Peng, R.; Yang, Y.; Ju, Y.; Mao, L.; Yang, Y. Computation of fractal dimension of rock pores based on gray CT images. *Chin. Sci. Bull.* **2011**, *56*, 3346. [CrossRef]
135. Schmitt Rahner, M.; Halisch, M.; Peres Fernandes, C.; Weller, A.; Sampaio Santiago dos Santos, V. Fractal dimensions of pore spaces in unconventional reservoir rocks using X-ray nano- and micro-computed tomography. *J. Nat. Gas. Sci. Eng.* **2018**, *55*, 298–311. [CrossRef]
136. Dong, E.; Jia, Z.; Jia, L.; Rao, S.; Zhao, X.; Yu, R.; Zhang, Z.; Gao, Y.; Wang, W.; Zhang, Y.; et al. Modeling fiber alignment in 3D printed ultra-high-performance concrete based on stereology theory. *Cem. Concr. Compos.* **2024**, *154*, 105786. [CrossRef]
137. Hiew, S.Y.; Teoh, K.B.; Raman, S.N.; Hung, C.-C.; Yoo, D.-Y.; Wen, K.-W.; Kong, D.; Voo, Y.L. 3D micro-CT driven fibre orientation–confinement correlation model for ultra-high-performance concrete (UHPC). *Cem. Concr. Compos.* **2025**, *161*, 106081. [CrossRef]
138. Oesch, T.; Landis, E.; Kuchma, D. A methodology for quantifying the impact of casting procedure on anisotropy in fiber-reinforced concrete using X-ray CT. *Mater. Struct.* **2018**, *51*, 73, Correction in *Mater. Struct.* **2019**, *52*, 44. https://doi.org/10.1617/s11527-019-1339-8. [CrossRef]
139. Okunishi, J.-I.; Uchida, Y.; Inaguma, H.; Tanaka, A. Evaluation of fiber orientation in UHPC members using X-ray micro-CT and estimation of member strength. In *Transforming Construction: Advances in Fiber Reinforced Concrete*; Mechtcherine, V., Signorini, C., Junger, D., Eds.; RILEM Bookseries; Springer: Cham, Switzerland, 2024; Volume 54, pp. 19–26. [CrossRef]
140. Ruan, T.; Poursaee, A. Fiber-distribution assessment in steel fiber–reinforced UHPC using conventional imaging, X-ray CT scan, and concrete electrical conductivity. *J. Mater. Civ. Eng.* **2019**, *31*, 04019133. [CrossRef]
141. Yang, Y.; Zhang, Y.; She, W.; Wu, Z.; Liu, Z.; Ding, Y. Nondestructive monitoring the deterioration process of cement paste exposed to sodium sulfate solution by X-ray computed tomography. *Constr. Build. Mater.* **2018**, *186*, 182–190. [CrossRef]

142. Wang, C.; Du, Z. Microscopic interface deterioration mechanism and damage behavior of high-toughness recycled aggregate concrete based on 4D in-situ CT experiments. *Cem. Concr. Compos.* **2024**, *153*, 105720. [CrossRef]
143. Ripley, B.D. Modelling spatial patterns. *J. R. Stat. Soc. Ser. B Methodol.* **1977**, *39*, 172–192. [CrossRef]
144. Paswan, R.; Das, S. Mechanistic links between multiscale pore network evolution and chloride transport in PCM-integrated concretes subjected to freeze–thaw cycling. *Cem. Concr. Compos.* **2026**, *173*, 106756. [CrossRef]
145. Das, S.; Yang, P.; Singh, S.S.; Mertens, J.C.E.; Xiao, X.; Chawla, N.; Neithalath, N. Effective properties of a fly ash geopolymer: Synergistic application of X-ray synchrotron tomography, nanoindentation, and homogenization models. *Cem. Concr. Res.* **2015**, *78*, 252–262. [CrossRef]
146. Al-Kharusi, A.S.; Blunt, M.J. Network extraction from sandstone and carbonate pore space images. *J. Pet. Sci. Eng.* **2007**, *56*, 219–231. [CrossRef]
147. Arand, F.; Hesser, J. Accurate and efficient maximal ball algorithm for pore network extraction. *Comput. Geosci.* **2017**, *101*, 28–37. [CrossRef]
148. Rabbani, A.; Ayatollahi, S.; Kharrat, R.; Dashti, N. Estimation of 3-D pore network coordination number of rocks from watershed segmentation of a single 2-D image. *Adv. Water Resour.* **2016**, *94*, 264–277. [CrossRef]
149. Huang, J.; Zhang, Y.; Sun, Y.; Ren, J.; Zhao, Z.; Zhang, J. Evaluation of pore size distribution and permeability reduction behavior in pervious concrete. *Constr. Build. Mater.* **2021**, *290*, 123228. [CrossRef]
150. Yu, F.; Sun, D.; Hu, M.; Wang, J. Study on the pores characteristics and permeability simulation of pervious concrete based on 2D/3D CT images. *Constr. Build. Mater.* **2019**, *200*, 687–702. [CrossRef]
151. Bernachy-Barbe, F.; Sayari, T.; Dewynter-Marty, V.; L'Hostis, V. Using X-ray microtomography to study the initiation of chloride-induced reinforcement corrosion in cracked concrete. *Constr. Build. Mater.* **2020**, *259*, 119574. [CrossRef]
152. Kim, K.Y.; Yun, T.S.; Park, K.P. Evaluation of pore structures and cracking in cement paste exposed to elevated temperatures by X-ray computed tomography. *Cem. Concr. Res.* **2013**, *50*, 34–40. [CrossRef]
153. Oesch, T.; Weise, F.; Bruno, G. Detection and quantification of cracking in concrete aggregate through virtual data fusion of X-ray computed tomography images. *Materials* **2020**, *13*, 3921. [CrossRef] [PubMed]
154. Nguyen, T.; Ghazlan, A.; Kashani, A.; Bordas, S.; Ngo, T. 3D meso-scale modelling of foamed concrete based on X-ray computed tomography. *Constr. Build. Mater.* **2018**, *188*, 583–598. [CrossRef]
155. Provis, J.L.; Myers, R.J.; White, C.E.; Rose, V.; van Deventer, J.S.J. X-ray microtomography shows pore structure and tortuosity in alkali-activated binders. *Cem. Concr. Res.* **2012**, *42*, 855–864. [CrossRef]
156. Skarżyński, Ł.; Kibort, K.; Małachowska, A. 3D X-ray micro-CT analysis of rebar corrosion in reinforced concrete subjected to a chloride-induced environment. *Molecules* **2021**, *27*, 192. [CrossRef] [PubMed]
157. de Almeida Ferreira, I.C.; Paciornik, S.; de Andrade Silva, F. Microstructural investigation of concretes with recycled aggregates using X-ray microtomography. *J. Build. Eng.* **2024**, *84*, 108487. [CrossRef]
158. Thomas, C.; Setién, J.; Polanco, J.A.; de Brito, J.; Fiol, F. Micro- and macro-porosity of dry- and saturated-state recycled aggregate concrete. *J. Clean. Prod.* **2019**, *211*, 932–940. [CrossRef]
159. Guo, L.-K.; Chen, L.-B.; Chen, Z.-W.; Wang, J.-Y. Enhancing UHPC tensile performance using polystyrene beads: Significant improvements and mechanisms. *Materials* **2024**, *17*, 2479. [CrossRef] [PubMed]
160. Lu, H.; Alymov, E.; Shah, S.; Peterson, K. Measurement of air void system in lightweight concrete by X-ray computed tomography. *Constr. Build. Mater.* **2017**, *152*, 467–483. [CrossRef]
161. Zhang, Y.; Qiao, H.; Qian, R.; Xue, C.; Feng, Q.; Su, L.; Zhang, Y.; Liu, G.; Du, H. Relationship between water transport behaviour and interlayer voids of 3D printed concrete. *Constr. Build. Mater.* **2022**, *326*, 126731. [CrossRef]
162. Zhang, Y.; Yang, L.; Qian, R.; Liu, G.; Zhang, Y.; Du, H. Interlayer adhesion of 3D printed concrete: Influence of layer stacked vertically. *Constr. Build. Mater.* **2023**, *399*, 132424. [CrossRef]
163. Lanzón, M.; Cnudde, V.; de Kock, T.; Dewanckele, J. X-ray microtomography (μ-CT) to evaluate microstructure of mortars containing low density additions. *Cem. Concr. Compos.* **2012**, *34*, 993–1000. [CrossRef]
164. Wan, K.; Xu, Q. Local porosity distribution of cement paste characterized by X-ray micro-tomography. *Sci. China Technol. Sci.* **2014**, *57*, 953–961. [CrossRef]
165. Wang, Y.-S.; Dai, J.-G. X-ray computed tomography for pore-related characterization and simulation of cement mortar matrix. *NDT E Int.* **2017**, *86*, 28–35. [CrossRef]
166. Yang, Z.; Dong, S.; Zhang, Y. Particle packing optimization and pore structure assessment of ternary cementitious system based on X-ray computed tomography and mercury intrusion porosimetry. *Constr. Build. Mater.* **2024**, *413*, 134913. [CrossRef]
167. Ševčík, R.; Adámková, I.; Vopálenský, M.; Martauz, P.; Šmilauer, V. Microcrack and porosity development in sealed cement mortars measured with micro-computed tomography. *Materials* **2024**, *17*, 3239. [CrossRef] [PubMed]
168. Thomoglou, A.K.; Fantidis, J.G.; Voutetaki, M.E.; Metaxa, Z.S.; Chalioris, C.E. Mechanical characterization of nano-reinforced mortar: X-ray micro-CT for 3D imaging of microstructure. *Eng. Proc.* **2023**, *41*, 4. [CrossRef]

169. Cui, X.; Zhang, X.; Wang, J.; Zhang, J.; Qi, H.; Li, J. X-ray CT based clogging analyses of pervious concrete pile by vibrating-sinking tube method. *Constr. Build. Mater.* **2020**, *262*, 120075. [CrossRef]
170. Ekolu, S.O.; Solomon, F.; de Beer, F.; Bitandi, L.; Kilula, R.N.; Maseko, K.T.; Mahlangu, F.G. Measurement of pore volume, connectivity and clogging of pervious concrete reactive barrier used to treat acid mine drainage. *Environ. Sci. Pollut. Res.* **2022**, *29*, 55743–55756. [CrossRef] [PubMed]
171. Batool, F.; Bindiganavile, V. Microstructural parameters of fiber reinforced cement-based foam and their influence on compressive and thermal properties. *J. Build. Eng.* **2020**, *31*, 101320. [CrossRef]
172. Shi, F.; Li, T.; Wang, W.; Liu, R.; Liu, X.; Tian, H.; Liu, N. Research on the effect of desert sand on pore structure of fiber reinforced mortar based on X-CT technology. *Materials* **2021**, *14*, 5572. [CrossRef] [PubMed]
173. Vicente, M.A.; Mínguez, J.; González, D.C. Variation of the pore morphology during the early age in plain and fiber-reinforced high-performance concrete under moisture-saturated curing. *Materials* **2019**, *12*, 975. [CrossRef] [PubMed]
174. Ponikiewski, T.; Katzer, J.; Bugdol, M.; Rudzki, M. X-ray computed tomography harnessed to determine 3D spacing of steel fibres in self compacting concrete (SCC) slabs. *Constr. Build. Mater.* **2015**, *74*, 102–108. [CrossRef]
175. Kaczmarczyk, G.P.; Kinasz, R.; Bilozir, V.; Bidenko, I. Application of X-ray computed tomography to verify bond failures mechanism of fiber-reinforced fine-grain concrete. *Materials* **2022**, *15*, 2193. [CrossRef] [PubMed]
176. Zhu, C.; Zhu, E.; Wang, B.; Li, J.; Yao, T.; Zhang, Z. Effect of porosity and pore size on the axial compressive properties of recycled aggregate concrete. *Materials* **2025**, *18*, 2830. [CrossRef] [PubMed]
177. Vásárhelyi, L.; Sebők, D.; Szenti, I.; Szép, O.; Kónya, Z.; Kukovecz, Á. Unlocking concrete's three-dimensional pore structure: A comprehensive micro-CT analysis. *Mater. Struct.* **2026**, *59*, 117. [CrossRef]
178. Taheri-Shakib, J.; Al-Mayah, A. Corrosion-induced cracking in reinforced concrete: The role of concrete cover thickness. *Mater. Struct.* **2025**, *58*, 288. [CrossRef]
179. Yu, F.; Chen, M.; Zhou, M.; Yang, Q.; Xie, H.; Yin, H.; Li, W.; Poon, C.S.; Liu, F. Study on corrosion characteristics of steel rebars and corrosion-induced cracks in reinforced concrete by employing X-ray microcomputed tomography. *J. Build. Eng.* **2025**, *100*, 111738. [CrossRef]
180. Guo, S.; Dai, Q.; Sun, X.; Xiao, X. X-ray CT characterization and fracture simulation of ASR damage of glass particles in alkaline solution and mortar. *Theor. Appl. Fract. Mech.* **2017**, *92*, 76–88. [CrossRef]
181. Kim, T.; Alnahhal, M.F.; Nguyen, Q.D.; Panchmatia, P.; Hajimohammadi, A.; Castel, A. Initial sequence for alkali-silica reaction: Transport barrier and spatial distribution of reaction products. *Cem. Concr. Compos.* **2019**, *104*, 103378. [CrossRef]
182. Yang, S.; Zheng, D.; Poon, C.S.; Cui, H. In-situ alkali–silica reaction evolution of lightweight aggregate concretes prepared with alkali-activated cement and ordinary Portland cement assessed by X-ray micro computed-tomography. *Cem. Concr. Compos.* **2023**, *140*, 105108. [CrossRef]
183. Liu, C.; Liu, H.; Wu, Y.; Wu, J.; Ding, S. Effect of X-ray CT characterized pore structure on the freeze–thaw resistance of 3D printed concrete with recycled coarse aggregate. *Constr. Build. Mater.* **2025**, *469*, 140492. [CrossRef]
184. Aziz, I.H.A.; Abdullah, M.M.A.B.; Razak, R.A.; Yahya, Z.; Salleh, M.A.A.M.; Chaiprapa, J.; Rojviriya, C.; Vizureanu, P.; Sandu, A.V.; Tahir, M.F.; et al. Mechanical performance, microstructure, and porosity evolution of fly ash geopolymer after ten years of curing age. *Materials* **2023**, *16*, 1096. [CrossRef] [PubMed]
185. Kovářík, T.; Hájek, J.; Hervert, T.; Deshmukh, K.; Pola, M.; Jansa, Z.; Beneš, J.; Svoboda, M. Silica-based geopolymer spherical beads: Influence of viscosity on porosity architecture. *Cem. Concr. Compos.* **2021**, *124*, 104261. [CrossRef]
186. Li, R.; Wu, G.; Jiang, L.; Sun, D. Characterization of multi-scale porous structure of fly ash/phosphate geopolymer hollow sphere structures: From submillimeter to nano-scale. *Micron* **2015**, *68*, 54–58. [CrossRef] [PubMed]
187. Jaji, M.B.; van Zijl, G.P.A.G.; Babafemi, A.J. Durability and pore structure of metakaolin-based 3D printed geopolymer concrete. *Constr. Build. Mater.* **2024**, *422*, 135847. [CrossRef]
188. Adrien, J.; Elsayed, H.; Gobbin, F.; Italiano, A.; Maire, E.; Colombo, P. X-ray computed tomography investigation on the geopolymer matrix formation during the binder jetting additive manufacturing process. *Addit. Manuf.* **2025**, *109*, 104852. [CrossRef]
189. Bayat, H.; Karimpouli, S.; Yang, L.; Ramandi, H.L.; Kashani, A. Investigation of interlayer bonding and pore characteristics in 3D-printed high-strength mortar incorporating recycled lightweight aggregates. *J. Build. Eng.* **2025**, *103*, 112183. [CrossRef]
190. Gupta, S.; Ghantous, R.M.; Weiss, W.J.; Moini, R. Pore connectivity and arrangement in additively manufactured cementitious material. *Cem. Concr. Res.* **2026**, *204*, 108206. [CrossRef]
191. Hou, S.; Duan, Z.; Ye, T.; Zou, S.; Xiao, J. Mechanical properties and pore structure of 3D printed mortar with recycled powder. *Constr. Build. Mater.* **2023**, *394*, 132068. [CrossRef]
192. Zhao, Y.; Shen, G.; Zhu, L.; Ding, Y.; Guan, X. Enhancing interfacial bonding and pore structure optimization in 3D-printed high-strength ECC with steel-PE hybrid fibers. *Case Stud. Constr. Mater.* **2025**, *23*, e04934. [CrossRef]
193. Heck, L.; Leutbecher, T. 3D-characterization of fibers in UHPFRC by computed tomography and photography. *Constr. Build. Mater.* **2025**, *483*, 141659. [CrossRef]

194. Luo, X.; Matsumoto, T. Tensile strength estimation of UHPFRC based on predicted cracking location using deep learning. *Materials* **2025**, *18*, 2237. [CrossRef] [PubMed]
195. Cai, M.; Zhu, H.; Rabczuk, T.; Zhuang, X. Mixer influence on pore characteristics and fiber dispersion in engineered cementitious composites across various strength grades. *Constr. Build. Mater.* **2025**, *467*, 140380. [CrossRef]
196. Li, Z.; Yu, J.; Zhou, J.; Leung, C.K.Y. Meso-level pore structures of strain-hardening cementitious composites (SHCC): Correlation with matrix flowability and application in micromechanical modeling. *Cem. Concr. Res.* **2026**, *199*, 108039. [CrossRef]
197. Lorenzoni, R.; Tinoco, M.; Paciornik, S.; de Andrade Silva, F. The use of X-ray microtomography to investigate the shear behavior of hybrid fiber reinforced strain hardening cementitious composites. *J. Build. Eng.* **2021**, *43*, 103126. [CrossRef]
198. Song, H.; Kim, T.; Hajimohammadi, A.; Oh, J.E.; Castel, A. Detailed characterisation of hemp and hempcrete pore structures: Effects on thermal and acoustic properties. *Cem. Concr. Res.* **2024**, *186*, 107702. [CrossRef]
199. Anders, N. Investigations about porosity analyzing of AAC. *ce/papers* **2018**, *2*, 141–145. [CrossRef]
200. Bumanis, G.; Vitola, L.; Zhou, X.; Vaičiukynienė, D.; Bajare, D. Towards 3D pore structure of porous gypsum cement pozzolan ternary binder by micro-computed tomography. *J. Compos. Sci.* **2024**, *8*, 264. [CrossRef]
201. Chung, S.-Y.; Abd Elrahman, M.; Kim, J.-S.; Han, T.-S.; Stephan, D.; Sikora, P. Comparison of lightweight aggregate and foamed concrete with the same density level using image-based characterizations. *Constr. Build. Mater.* **2019**, *211*, 988–999. [CrossRef]
202. Chung, S.-Y.; Kim, J.-S.; Han, T.-S.; Stephan, D.; Kamm, P.H.; Abd Elrahman, M. Characterization of foamed concrete with different additives using multi-scale micro-computed tomography. *Constr. Build. Mater.* **2022**, *319*, 125953. [CrossRef]
203. Bentz, D.P.; Quenard, D.A.; Kunzel, H.M.; Baruchel, J.; Peyrin, F.; Martys, N.S.; Garboczi, E.J. Microstructure and transport properties of porous building materials. II: Three-dimensional X-ray tomographic studies. *Mater. Struct.* **2000**, *33*, 147–153. [CrossRef]
204. Korat, L.; Ducman, V.; Legat, A.; Mirtič, B. Characterisation of the pore-forming process in lightweight aggregate based on silica sludge by means of X-ray micro-tomography (micro-CT) and mercury intrusion porosimetry (MIP). *Ceram. Int.* **2013**, *39*, 6997–7005. [CrossRef]
205. Lee, A.H.; Moore, J.M.; Covarrubias, B.V.; Lynch, L.M. Segmentation of cortical bone, trabecular bone, and medullary pores from micro-CT images using 2D and 3D deep learning models. *Anat. Rec.* **2025**, *308*, 3082–3104. [CrossRef] [PubMed]
206. Cole, M.E.; Stout, S.D.; Dominguez, V.M.; Agnew, A.M. Pore Extractor 2D: An ImageJ toolkit for quantifying cortical pore morphometry on histological bone images, with application to intraskeletal and regional patterning. *Am. J. Biol. Anthropol.* **2022**, *179*, 365–385. [CrossRef]

Disclaimer/Publisher's Note: The statements, opinions and data contained in all publications are solely those of the individual author(s) and contributor(s) and not of MDPI and/or the editor(s). MDPI and/or the editor(s) disclaim responsibility for any injury to people or property resulting from any ideas, methods, instructions or products referred to in the content.